AIRCRAFT OBSERVATIONS OF SUB-CLOUD AEROSOL AND CONVECTIVE CLOUD PHYSICAL PROPERTIES

A Thesis

by

DUNCAN AXISA

Submitted to the Office of Graduate Studies of
Texas A&M University
in partial fulfillment of the requirements for the degree of

MASTER OF SCIENCE

December 2009

Major Subject: Atmospheric Sciences

AIRCRAFT OBSERVATIONS OF SUB-CLOUD AEROSOL AND CONVECTIVE CLOUD PHYSICAL PROPERTIES

A Thesis

by

DUNCAN AXISA

Submitted to the Office of Graduate Studies of
Texas A&M University
in partial fulfillment of the requirements for the degree of

MASTER OF SCIENCE

Approved by:

Chair of Committee,	Don R. Collins
Committee Members,	Sarah D. Brooks
	Simon W. North
Head of Department,	Kenneth Bowman

December 2009

Major Subject: Atmospheric Sciences

ABSTRACT

Aircraft Observations of Sub-Cloud Aerosol and Convective Cloud Physical Properties.

(December 2009)

Duncan Axisa, B.Ed., University of Malta; B.S., Texas A&M University

Chair of Advisory Committee: Dr. Don Collins

This research focuses on aircraft observational studies of aerosol-cloud interactions in cumulus clouds. The data were collected in the summer of 2004, the spring of 2007 and the mid-winter and spring of 2008 in Texas, central Saudi Arabia and Istanbul, Turkey, respectively. A set of 24 pairs of sub-cloud aerosol and cloud penetration data are analyzed. Measurements of fine and coarse mode aerosol concentrations from 3 different instruments were combined and fitted with lognormal distributions. The fit parameters of the lognormal distributions are compared with cloud droplet effective radii retrieved from 260 cloud penetrations. Cloud condensation nuclei (CCN) measurements for a subset of 10 cases from the Istanbul region are compared with concentrations predicted from aerosol size distributions. Ammonium sulfate was assumed to represent the soluble component of aerosol with dry sizes smaller than 0.5 μm and sodium chloride for aerosol larger than 0.5 μm. The measured CCN spectrum was used to estimate the soluble fraction.

The correlations of the measured CCN concentration with the predicted CCN concentration were strong ($R^2 > 0.89$) for supersaturations of 0.2, 0.3 and 0.6%. The

measured concentrations were typically consistent with an aerosol having a soluble fraction between roughly 0.5 and 1.0, suggesting a contribution of sulfate or some other similarly soluble inorganic compound. The predicted CCN were found to vary by ±3.7% when the soluble fraction was varied by 0.1.

Cumulative aerosol concentrations at cutoff dry diameters of 1.1, 0.1 and 0.06 μm were found to be correlated with cloud condensation nuclei concentrations but not with maximum cloud base droplet concentrations. It is also shown that in some cases the predominant mechanisms involved in the formation of precipitation were altered and modified by the aerosol properties.

This study suggests that CCN-forced variations in cloud droplet number concentration can change the effective radius profile and the type of precipitation hydrometeors. These differences may have a major impact on the global hydrological cycle and energy budget.

DEDICATION

This manuscript is dedicated to my family, especially my wife Marietta, who has supported me through the process of conducting this research. I also dedicate this work to my mum who passed away on Christmas day of 2005.

ACKNOWLEDGEMENTS

I would like to thank my advisor, Dr. Don Collins, for guiding me during my research. I greatly appreciate his support during the field campaigns. I also value the encouragement of my co-workers at NCAR, especially Dr. Roelof Bruintjes and Dr. Paul Kucera. Furthermore, I would like to express my thanks to my colleagues Dr. Runjun Li, Crystal Reed, Chance Spencer, Nathan Taylor and Jason Tomlinson at Texas A&M University for their ideas and support throughout this work. I would also like to thank Dr. Sarah Brooks and Dr. Simon North for serving on the thesis committee. Special thanks go to Dr. Amit Teller, Dr. William Woodley and Dr. Daniel Rosenfeld for providing valuable insight into the conduct of this research. George Bomar was very supportive of my efforts during the initial phases of this work. Last but not least, I would like to thank the Board of Directors of the Sandy Land Underground Water Conservation District and its General Manager Gary Walker, for encouraging me and enabling me with the tools to conduct my research.

These field projects were supported by the Texas Department of Licensing and Regulation, the Presidency of Meteorology and Environment of Saudi Arabia and the Istanbul Metropolitan Municipality of Turkey.

TABLE OF CONTENTS

LIST OF FIGURES

FIGURE Page

FIGURE Page

FIGURE Page

LIST OF TABLES

1. INTRODUCTION

Atmospheric aerosol particles are an integral part of the atmospheric hydrological cycle and the atmospheric radiation budget. Aerosols affect the global energy budget both directly by scattering of radiation and indirectly by acting as cloud condensation nuclei (CCN). Aerosols scatter and absorb sunlight (direct effect) and change the microphysical structure, lifetime, and coverage of clouds (indirect effect). An increase in aerosol concentration leads to cloud droplets of a smaller size and higher cloud albedo (Twomey, 1977). This effect, which is referred to as the first aerosol indirect effect, tends to cool the global climate. The smaller cloud droplet size lowers collection efficiencies among droplets, delaying the formation of drizzle, leading to an expected increase in cloud coverage (aerosol second indirect effect (Albrecht, 1989)). The radiative impact of anthropogenic aerosol suppresses surface heating and evaporation and stabilizes the lower troposphere. Absorption of solar radiation by black carbon within and above the boundary layer can reduce cloud cover or inhibit cloud formation. This effect is termed the “semi-direct" aerosol effect (Hansen et al., 1997, Ackerman et al., 2000). The inhibition of cloud formation effectively reduces rainfall resulting in a slower hydrological cycle (Ramanathan, et al., 2001 and Rosenfeld, et al., 2008a).

Aerosol-induced precipitation suppression was suggested by the study of shallow stratiform clouds. Enhanced aerosol concentrations suppress warm rain by producing a narrow droplet spectrum that inhibits collision and coalescence processes (e.g., Squires and Twomey, 1960; Warner and Twomey, 1967 and Warner, 1968). A combination of

---

This thesis follows the style of *Journal of Applied Meteorology and Climatology.*

cloud top temperature and droplet effective radius, estimated from instrumented satellite platforms, has been used to infer the suppression of coalescence and precipitation processes from smoke (Rosenfeld and Lensky, 1998) and desert dust (Rosenfeld et al., 2001). Rosenfeld et al. (2008b) showed that aircraft measurements of cloud properties validated the satellite inferences of cloud microphysics in orographic clouds in the California Sierra Nevada. The analysis of several hundred cloud penetrations made by the research aircraft show that in regions where high concentrations of CCN were measured the orographic clouds had to grow to greater depths to develop precipitation than clouds growing in regions of low CCN concentrations. These observations supported previous analysis of a decreasing trend in orographic precipitation in the central and southern Sierra Nevada (Rosenfeld and Givati, 2006). Decreasing trends of upslope precipitation for elevated sites relative to upwind polluted sites were also found in Denver and Colorado Springs resulting in precipitation losses on the order of 1 mm yr^{-1} to the west of these cities (Jirak and Cotton, 2006). Alpert et al. (2008) argue that this decreasing trend is not because of precipitation suppression on the mountain but because of increases in precipitation downwind of the city, possibly due to urban heat island, surface roughness, humidity and various aerosol effects.

Observations of increased aerosol concentration are not easily related to an exact physical description of the active microphysical processes within clouds. When anthropogenic aerosol is added to the preexisting aerosol background, the aerosol size distribution is modified. In most cases this results in an increase in the number of CCN and cloud droplet number concentrations. A modification of the cloud base droplet number concentration and size distribution creates a perturbation in the cloud physics that

cannot be explained exactly. Numerous in-situ measurements show that anthropogenic aerosol influences the cloud microphysical processes (e.g. Hudson and Yum, 2001; Heymsfield and McFarquhar, 2001; Yum and Hudson, 2002; Andreae et al., 2004; Freud et al., 2008; Rosenfeld et al., 2008b; and many more). The physical description of the chain of events that lead to rainfall suppression is complex, involving interactions of dynamical as well as microphysical processes. In contrast to most of the sub-micron aerosols that act as CCN, giant CCN (GCCN, e.g., sea salt) are suggested to have an enhancing effect on the formation of precipitation (i.e., drizzle) (Rosenfeld et al., 2002). GCCN are aerosol particles larger than 2–5 μm in radius that can act as CCN. Some numerical models that simulate the development of single clouds show that without the presence of GCCN a high concentration of small nuclei tends to reduce precipitation (e.g. Yin et al., 2000; Levin et al., 2005 and Teller and Levin, 2006). However, other models that treat the dynamical processes in more detail show that the interactions between cloud microphysical processes and dynamics sometimes lead to precipitation suppression while under different meteorological conditions rainfall is enhanced (e.g. van den Heever et al. 2006; van den Heever and Cotton 2007 and Tao et al., 2007). Unfortunately, there are very few in situ measurements that link the microphysical parameters to changes in precipitation on the ground. Precipitation is a key atmospheric process in the global water cycle and a proxy variable in climate change research. Proper assessment of the impact of aerosol loading on precipitation has become increasingly important in ongoing climate diagnostics, numerical prediction and fresh-water resource management.

In various parts of the world policy makers have noted the results from many observations and model simulations of the effects of aerosols on clouds and the potential

effects on precipitation. Several field campaigns have been planned with the objective to measure aerosol properties under cloud bases and characterize the cloud microphysical properties and precipitation formation mechanisms. In this work field campaigns in Texas, Saudi Arabia and Turkey are discussed. The common goals of the field efforts were:

1. Retrieve the aerosol size distribution below the bases of convective clouds to study the CCN activation properties.
2. Describe the physical chain of events and the microphysical properties of cloud processes that lead to precipitation formation within convective clouds.

To satisfy these goals, instrumented aircraft were used to measure aerosol, cloud and precipitation properties. This study will present a description of the measurements obtained by the aircraft. The focus of the analysis is on comparisons between aerosols and the microphysical properties of convective clouds. Information on the vertical distribution of cloud droplet microphysics are compared with physical properties of the aerosols to provide insight on how these particles are affecting cloud properties with implications to cloud lifetime and precipitation. This study will not attempt to link the microphysical properties of clouds to the onset or production of precipitation. This type of analysis would require additional observations of precipitation particle size distributions, which were not made in all of the field projects discussed here.

The present study has 3 objectives. (1) To identify typical aerosol size distributions at cloud base and to characterize the variability of the size distribution. (2) To examine the CCN activation of aerosols as a function of the aerosol size distribution.

(3) The last objective is to provide information about the relationship between the droplet effective radius and the height above cloud base in different aerosol regimes.

2. FIELD CAMPAIGNS AND INSTRUMENTATION

Clouds were measured during three intensive studies carried out in the summer of 2004, the spring of 2007 and the mid-winter and spring of 2008 in Texas, central Saudi Arabia and Istanbul, Turkey, respectively. Cumuliform clouds were sampled under both warm and supercooled conditions. Cumulus clouds were characterized by flying several successively higher constant altitude cloud penetrations, starting with orbits below cloud base to obtain the aerosol properties and thermodynamic state of the air entrained through cloud base. The aircraft pilots used on-board cloud radar to avoid areas of precipitation, associated downdrafts and large hail. The flight scientist assisted the pilot by vectoring the aircraft to areas of new growth within organized convection. Therefore most of the cloud penetrations were done in growing cumulus towers, which restricts the data set to non-precipitating water clouds. Figure 1 shows a schematic of the aircraft profile used for each measurement flight.

Because the objective is to relate properties of aerosols measured below cloud base with cloud microphysical properties at varying cloud depth, the analysis was limited to cases with well-mixed conditions. During the three field campaigns 20 flights were dedicated to this strategy, during which 24 clouds were profiled resulting in 260 cloud penetrations (Table 1). These flights were conducted over land in Texas and Saudi Arabia. In Istanbul most of the flights were over land but occasionally over the coastal

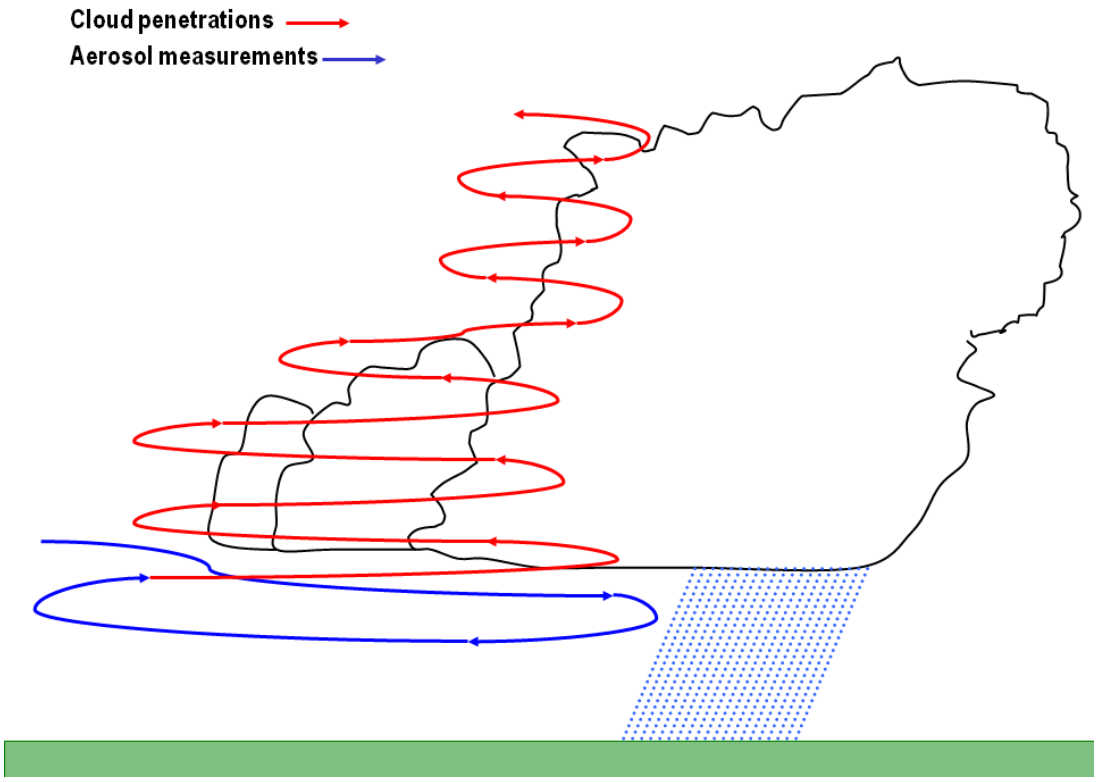

Figure 1. Schematic of the aircraft profile used during measurements.

area of the Black Sea and Sea of Marmara. Figures 2 to 6 show the geographical region where the measurements were made, the flight tracks of the measurement flights and the area where the clouds were sampled. These data provide a wide range of aerosol properties necessary to evaluate aerosol effects on cumulus microphysics.

The instrumented aircraft in Texas and Istanbul was the Seeding Operations and Atmospheric Research (SOAR) Piper Cheyenne II while that in Saudi Arabia was the Weather Modification Inc. (WMI) Piper Cheyenne II. Hereinafter these aircraft are referred to as the SOAR Cheyenne and WMI Cheyenne, respectively. Measurements of

Table 1. Date, cloud base altitude (h), pressure (P) and temperature (T) for the 24 clouds studied here.

Date (YYYYMMDDC†)	Cloud base h (m)	Cloud base P (mbar)	Cloud base T (°C)	Number of penetrations	Cloud depth (m)	Cloud type	Project
20040826C1	2835	726	19	10	1781	Shallow mixed phase Cu	Texas
20040827C2	2409	763	22	5	994	Shallow mixed phase Cu	
20040827C3	2250	779	21	10	2596	Deep mixed phase Cu	
20040828C4	2299	777	18	11	1545	Shallow mixed phase Cu	
20040902C5	2291	773	14	8	1526	Shallow mixed phase Cu	
20040902C6	2292	774	10	17	2763	Deep mixed phase Cu	
20040904C7	3506	670	5	11	1864	Shallow mixed phase Cu	
20040905C8	2550	751	14	14	2767	Deep mixed phase Cu	
20070405C9	3355	691	7	11	1563	Shallow mixed phase Cu	Riyadh, Saudi Arabia
20070407C10	4201	624	2	8	1707	Shallow mixed phase Cu	
20070408C11	4541	595	-1	6	1297	Shallow mixed phase Cu	
20070409C12	4359	606	0	7	1465	Shallow mixed phase Cu	
20070411C13	3500	673	5	6	627	Shallow mixed phase Cu	
20080203C14	1271	885	4	10	1196	Shallow mixed phase CuSc	Istanbul, Turkey
20080204C15	1000	913	7	11	1390	Shallow mixed phase CuSc	
20080319C16	1895	803	1	9	998	Shallow mixed phase Cu	
20080404C17	2102	784	-1	9	1595	Shallow mixed phase Cu	
20080405C18	1243	873	5	9	1220	Shallow mixed phase Cu	
20080416C19	1078	888	6	18	2320	Deep mixed phase Cu	
20080416C20	1078	888	6	21	2616	Deep mixed phase Cu	
20080606C21	949	908	16	15	1486	Shallow mixed phase Cu	
20080606C22	1141	887	15	13	2415	Deep mixed phase Cu	
20080607C23	1222	878	10	15	1985	Deep mixed phase Cu	
20080607C24	910	912	14	19	2590	Deep mixed phase Cu	

† is the cloud number; Cu = cumulus; Sc = stratocumulus

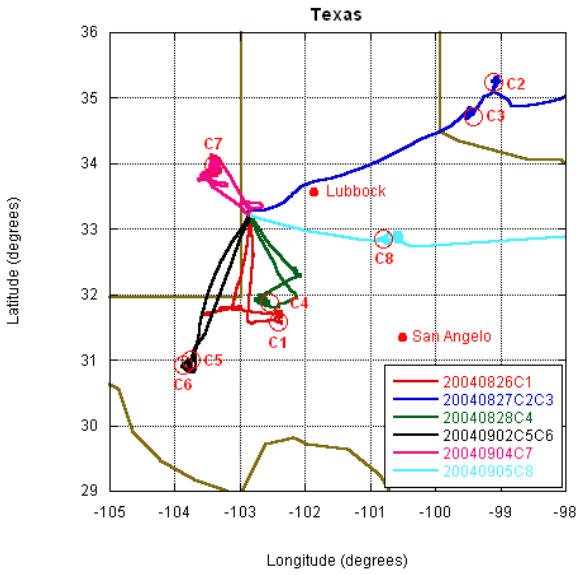

Figure 2. Flight tracks and areas where clouds were sampled in Texas and surrounding states.

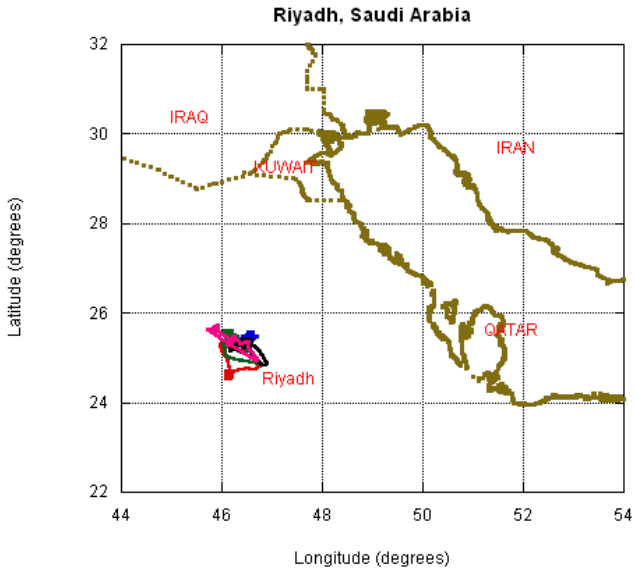

Figure 3. Flight tracks and the geographical area where the measurements were made in Saudi Arabia.

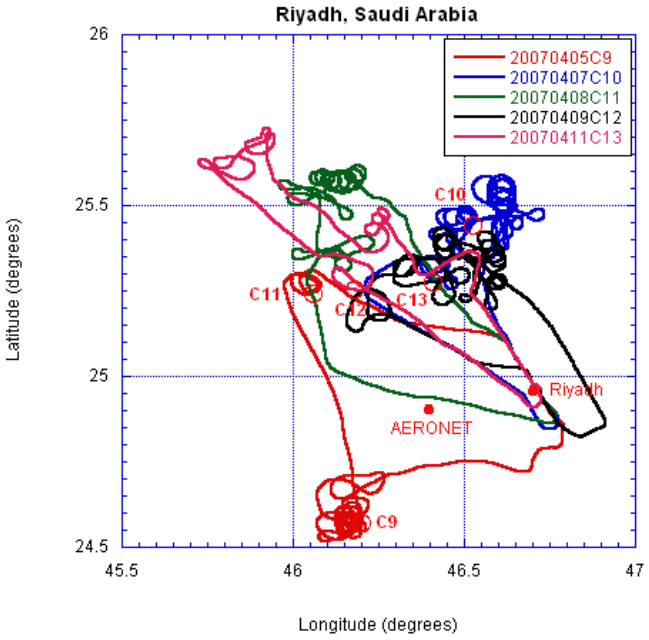

Figure 4. As in Figure 2 but in Riyadh, Saudi Arabia.

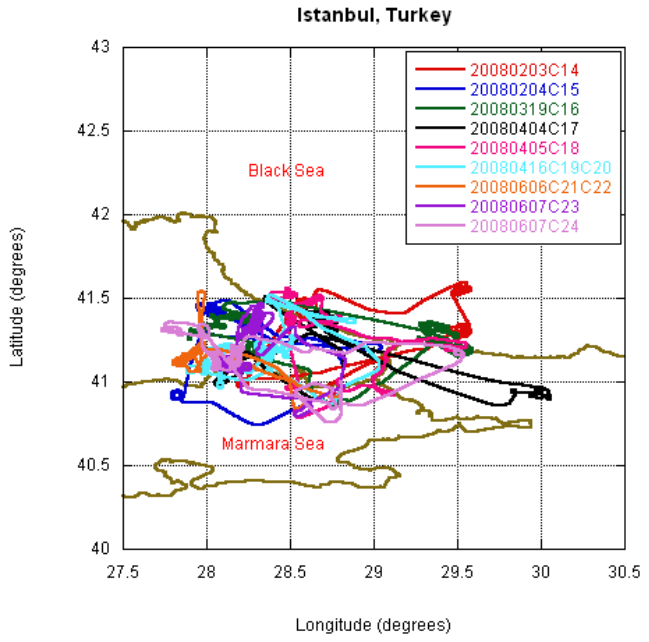

Figure 5. As in Figure 3 but in Istanbul, Turkey.

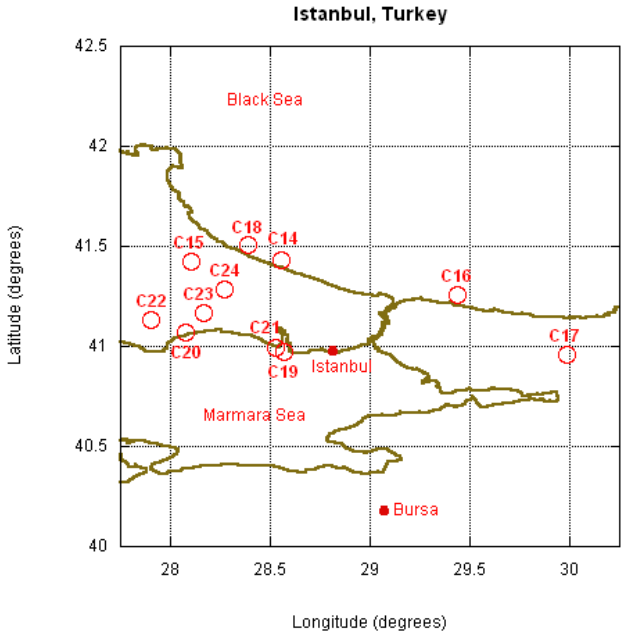

Figure 6. Areas where clouds were sampled in and around Istanbul, Turkey.

the aerosol size distribution (ASD) and the cloud droplet size distribution (DSD) were made continuously with instrumentation installed on the aircraft. The aerosol measurements were made by the Texas A&M University Differential Mobility Analyzer (DMA), the Particle Measuring Systems (PMS) Passive Cavity Aerosol Spectrometer Probe (PCASP), the Particle Measuring Systems (PMS) Forward Scatter Spectrometer Probe (FSSP-100) and the Droplet Measurement Technologies (DMT) Cloud Droplet Probe (CDP). CCN measurements were made by the DMT single column CCN counter.

The optical probe measurements were made by the CDP and PCASP SPP-200 in Texas and Istanbul and by the FSSP-100 and PCASP-100 in Saudi Arabia. The SOAR Cheyenne was also equipped with the Cloud Imaging Probe (CIP) and the Aircraft

Integrated Meteorological Measurement System (AIMMS). The PCASP, CDP, FSSP, CIP and AIMMS were wing mounted while the DMA and CCN counter were installed inside the aircraft cabin and sampled aerosols through an aerosol inlet mounted on the aircraft fuselage. The internal navigation and GPS positioning system were used to determine the altitude and position of the aircraft. The aircraft configuration and instrumentation is shown in Figures 7 to 10. The instrumentation payload for each intensive field campaign is listed in Table 2.

Aerosol number concentration (N) and diameter (D) were measured using two techniques to cover the 0.01 to 10 μm diameter range of interest. The DMA measured the aerosol number-size distributions, dN/dlog D (cm^{-3}), in the range 0.01 to 0.4 μm every 90 sec. The core of the DMA system is the Aerosol Dynamics Inc. high flow DMA (Stolzenburg et al., 1998). This DMA system is suitable for aircraft measurements as it operates at a higher sample flow rate of 1.5 L/min resulting in improved counting statistics. The DMA was operated in scanning mode to continuously vary the size of the separated particles. The selected particles were passed to a condensation particle counter (TSI CPC) for determining particle number concentration.

Optical probe measurements were made every second. In optical probes, the amount of light scattered by the sampled particle is a function of its size, shape, and refractive index. The PCASP measured aerosol in the accumulation mode and coarse mode while the CDP and FSSP measured coarse mode aerosol. Cloud droplet size spectra and droplet concentrations were measured using the cloud droplet spectrometers (CDP or FSSP). The CDP measures droplet size using a forward scattering principle similar to the FSSP. The CDP has certain design improvements over the FSSP. The

(a) (b)

Figure 7. (a) The SOAR Cheyenne aircraft, (b) CIP probe and the CDP probe as configured on the SOAR Cheyenne.

(a) (b)

Figure 8. (a) AIMMS probe and PCASP, (b) forward facing twin-diffuser type aerosol inlet as configured on the SOAR Cheyenne.

(a) (b)

Figure 9. (a) FSSP probe, (b) PCASP probe as configured on the WMI Cheyenne.

Figure 10. (a) DMA system and CCN counter as configured on the WMI Cheyenne.

Table 2. Measurements made by the research aircraft.

Property measured	Size range	Instrument	Project
Aerosol particle size	0.01 to 0.4 μm	DMA and TSI CPC	Texas and Istanbul
Aerosol particle size	0.1 to 3 μm, 30 channels	PMS PCASP SPP-200	
CCN concentration		DMT CCN-100	
Aerosol and cloud droplet particle size	2 to 50 μm, 30 channels	DMT CDP	
Cloud hydrometeor size and image	25 to 1550 μm, 62 channels	DMT CIP	
Aerosol particle size	0.01 to 0.4 μm	DMA and TSI CPC	Riyadh
Aerosol particle size	0.1 to 3 μm, 15 channels	PMS PCASP-100	
CCN concentration		DMT CCN-100	
Aerosol and cloud droplet particle size	3 to 47 μm, 20 channels	DMT FSSP-100	

most significant of these is that the FSSP has an inlet while the CDP has an open path design which reduces drop shattering and ice splintering (D. Baumgardner, personal communication, 2009). The PCASP sizes particles based on particle light scattering (35 to 135°) in a 633 nm HeNe passive cavity laser (Liu et al., 1992). The inlet deicing heater for the PCASP was activated during each flight such that the instrument measured a dry particle size distribution (RH ~ 40%). The FSSP gives an ambient size distribution based on 633 nm light scattering in the 4 to 12° range (Dye and Baumgardner, 1984). The CDP uses a 658 nm laser and a solid angle of 4 to 12° for collecting forward scattered light. The CDP detector is masked with a rectangular slit so that it only detects scattered light from particles within a certain distance of the center of focus. Thus, any uncertainty in sizing by the CDP is related to the refractive index or particle shape.

The CIP is a diode array optical probe. An incident laser beam is focused on particles ranging in size from 25 to 1550 μm, which are optically magnified by a factor of 8, onto a 200 μm pitch, 64-element photo diode array. The CIP data is composed of a 1D

particle histogram and a 2D particle image. A quantitative analysis of the CIP is not presented in this study and its data is only used to identify regions with large droplets, cloud hydrometeors and precipitation.

The DMT CCN counter uses a 50-cm long cylindrical column continuous-flow streamwise thermal gradient chamber to generate a supersaturation maximum at the center of the column (Roberts and Nenes, 2005). Cloud droplets form on CCN and are counted with an optical particle counter (OPC) immediately downstream of the CCN column. The OPC uses a 660nm diode laser for the particle size and number concentration measurements. Droplets with sizes between 0.75 and 10 μm in diameter are counted as CCN.

Calibrations were conducted before and after deployment and are based on glass beads for the FSSP and CDP, polystyrene spheres for the PCASP and size-resolved dry aerosol distributions of $(NH_4)_2SO_4$ for the CCN counter. The CIP was calibrated by operating a glass spinning disc to simulate spherical particles streaming through the sampling area. The field calibrations for the PCASP and CDP suggest that the calibration remained stable. Some inconsistency in the FSSP calibration was found in Saudi Arabia. As a result the FSSP-100 probe was replaced with a newly calibrated FSSP-100. The erroneous FSSP data have been removed from the data set for this study. During instrument inter-comparisons between the DMA and the PCASP a consistent disagreement was found in the size distributions in the range 0.3 to 0.4 μm. This anomaly was found to be consistent between PCASP SPP-200 instruments, and is likely due to a gain shift in the instrument in the 0.3 to 0.5 μm range as suggested by Reid et al. (2003).

3. DATA ANALYSIS PROCEDURE: AEROSOL SIZE DISTRIBUTION

Observations of atmospheric aerosols indicate that aerosol size distributions reflect multiple aerosol populations, each originating from a distinct source region. ASDs are shaped by complex nonlinear processes that are difficult to represent numerically. These processes include nucleation of new particles and evaporation, growth and coagulation of existing particles. Most current models explicitly represent the ASD with either discrete size bins or with assumed functional forms for the shape of the distribution. Different assumptions have been applied in describing the shape of the distributions, e.g., histograms (Heintzenberg, 1978), gamma distributions (Tampieri and Tomasi, 1976), and lognormal functions (Birmili et al., 2001, Hussein et al., 2005 and Salma et al., 2005). In the latter case, one classic method used to simplify ASDs is that in which distributions are fit to three log-normal functions each to describe three modes; "nuclei," "accumulation," and "coarse," roughly corresponding to the size ranges below 0.1 μm, 0.1 to 1 μm, and above 1 μm, respectively (Willeke and Whitby, 1975). An additional Aitken particle mode is often identified between the nucleation and the accumulation particle modes. Thus four log-normal functions, three of which are in the sub-micrometer range, are often required to fit the entire size distribution. An example of an idealized size distribution with four log-normal functions is shown in Figure 11.

In most cases, aerosol observations were obtained separately for each cloud by determining the time period when the aircraft was at a constant altitude, between cloud base and 1 km below cloud base, and outside of precipitation. For the cloud pairs 20040827C2 and 20040827C3, 20040902C5 and 20040902C6, and 20080606C21 and

20080606C22, one ASD was used for each cloud pair. This was done because 2 clouds were sampled on each day and an ASD was not obtained between cloud measurements. Aerosol size measured by the DMA, the PCASP and the cloud droplet spectrometers (CDP or FSSP) in the sub-cloud legs was averaged and merged into a single size distribution to obtain the ASD. The averaging time ranged from 4 to 16 minutes with a mean of 10 minutes. A different DMA instrument was used in each field campaign. Although the DMAs were different, the aerosol concentration counting efficiency of the CPC can be assumed to be consistent between projects within the sizing range of the DMA. This cannot be assumed for the PCASP, CDP and FSSP. Three different PCASP instruments were used and no inter-comparison data exists between PCASP instruments. This is also the case with the CDP and FSSP. Although the CDP instrument used in Texas and Istanbul on the SOAR Cheyenne was the same instrument, a firmware upgrade was done on the CDP between field campaigns. There is also no inter-comparison data between the CDP and FSSP instruments used in this study.

The DMA data were processed using software developed by our research group. In this software, the raw DMA data is inverted and smoothed using a version of the Twomey algorithm derived from Twomey (1965, 1975) and Markowski (1987). The inversion of the raw data (particle counts versus DMA voltage or time) accounts for the presence of multiply-charged particles, the finite width of the DMA transfer function and particle loss in the instrument.

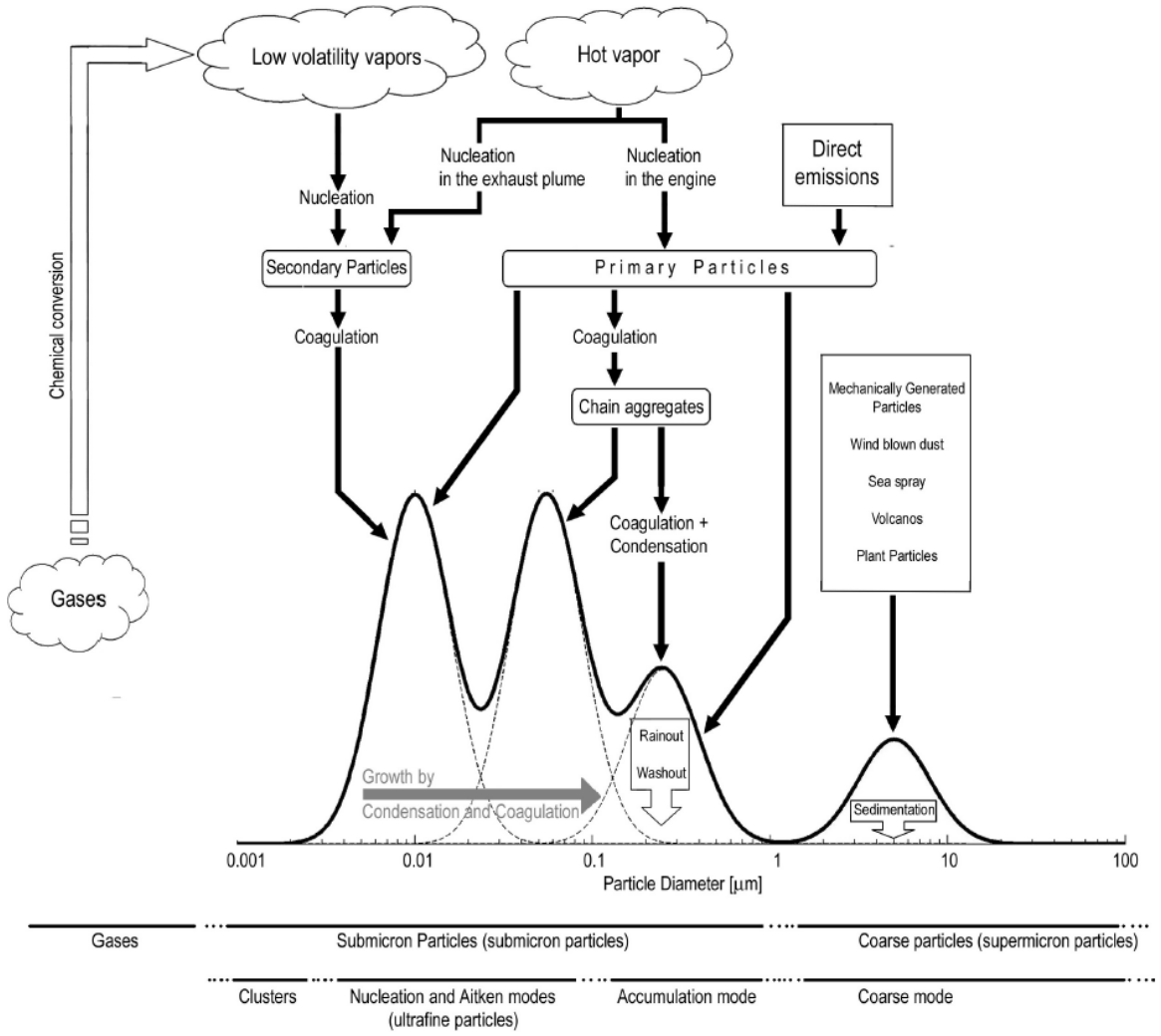

Figure 11. Idealized schematic of an atmospheric particle number size distribution. Principal modes, sources, and particle formation and removal mechanisms are indicated (Hussein et al., 2005).

The aerosol and cloud spectrometer data is processed by integrating the particle counts in each size bin and dividing the integrated counts by the sampling flow. In the case of the PCASP the sampling flow is measured by a flow meter inside the PCASP instrument and ranges from about 0.03 to 0.06 L/min during a research flight. The CCN

counter has a sampling flow of 0.05 L/min. The sampling flow in the CDP and FSSP is equal to the product of the view volume and the research aircraft airspeed which varies from 70 to 110 m/s for the Piper Cheyenne II.

A least squares fitting algorithm was used to parameterize the aerosol number size distributions by multiple lognormal functions. The use of four lognormal modes allows for better fitting of the narrow Aitken mode, two overlapping sub modes within the accumulation mode, and the broad "tail" of the coarse mode. The lognormal equation follows Reist (1984) and is given by

$$dN/d\log D = \text{Curve 1} + \text{Curve 2} + \text{Curve 3} + \text{Curve 4}$$

$$Curve X = \frac{N}{D \ln \sigma_g \sqrt{2\pi}} \exp\left[\frac{-(\ln D - \ln D_g)^2}{2 \ln^2 \sigma_g}\right] \qquad \text{Eq. 1}$$

where D is the diameter of an aerosol particle (μm), N is the total number concentration (cm^{-3}), σ_g is the geometric standard deviation, and D_g is the geometric mean diameter (μm). Constraints were applied to the lognormal fitting algorithm so that (1) any nucleation mode has a small geometric mean diameter smaller than 0.1 μm, (2) the coarse mode has a large standard deviation, (3) the mean square errors for both the number and volume distribution fits are minimized, (4) the addition of the individual lognormal distributions has a shape similar to the measured average, and (5) the fitting parameters are physically reasonable. Constraints were also imposed to the fitting procedure. For example, Clarke et al. (1997) applied a lognormal fit to the accumulation mode mass distribution and then applied a second lognormal fit to the nucleation mode using the

number distribution. In most cases, the nucleation, Aitken and accumulation mode were fit using the number size distribution while the coarse mode was fit using the volume size distribution. These constraints captured the modes more accurately after various fitting runs. Figure 12 shows an example of merging data from the DMA, PCASP and the cloud droplet spectrometers (CDP or FSSP) into a single size distribution. Figure 13 shows the four lognormal size distributions used to parameterize the aerosol number size distributions. Table 3 describes the fit parameters from an ASD obtained on 9 April 2007 in Riyadh Saudi Arabia at cloud base level in a dust storm.

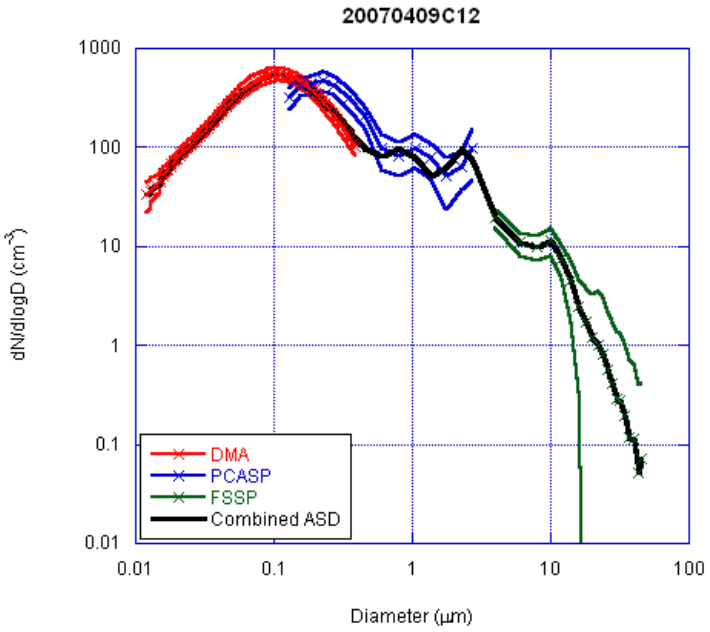

Figure 12. DMA data (middle red trace), PCASP data (middle blue trace) and FSSP data (middle green trace) are used to produce the combined ASD (black trace) for 9 April 2007. The traces above and below the middle trace indicate the spread in the data expressed as one standard deviation above and below the mean.

The parameters of the fitted lognormals (N, D_g and σ_g) contain all of the information in the size distributions and can be useful in aerosol classification based on size distribution data. Therefore, plots of the mode diameters can display the systematic characteristics of the size distributions. In chapter 6 the characteristics of the ASDs are correlated with the cloud penetration data to investigate whether a simple relationship exists between the ASD fit parameters and the cloud droplet effective diameter.

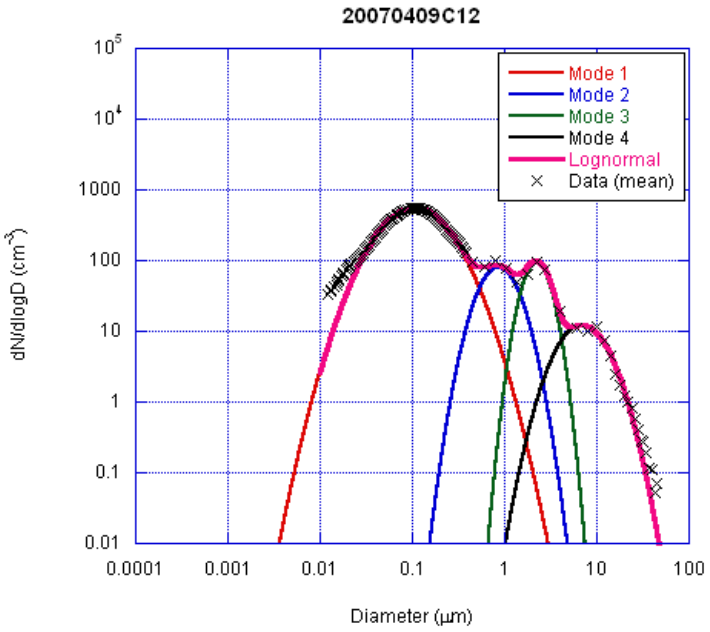

Figure 13. Lognormal fits are applied to the combined ASD obtained in Figure 12.

Table 3. Fit parameters for the ASD shown in Figure 13.

Mode number	N (cm^{-3})	D_g (µm)	σ_g	R^2
1	432.0	0.1	2.05	0.994
2	35.0	0.9	1.5	
3	28.5	2.2	1.3	
4	6.7	7.0	1.7	

4. DATA ANALYSIS PROCEDURE: CCN

One of the objectives of this study was to retrieve the ASD below the bases of convective clouds to study the CCN activation properties. The activation of aerosol particles as CCN is a crucial process in the dynamical and microphysical evolution of clouds. The number, size and hygroscopicity of aerosol particles as well as the updraft velocity are the main parameters that govern the CCN activation and initial cloud droplet growth (Reutter, 2009).

CCN data is described as number of CCN as a function of water vapor supersaturation. As mentioned before, CCN measurements were made with the DMT CCN counter at supersaturation varying from 0.2 to 0.6%. This range was chosen as maximum supersaturation in cumulus cloud rarely exceeds 0.8% (Pruppacher and Klett, 1997). During normal operation, the CCN was run at a constant supersaturation of 0.3%. Below cloud base the CCN was stepped through 3 supersaturation settings to obtain a supersaturation spectrum.

In order for a CCN particle to become a cloud droplet, a minimum water vapor supersaturation, or critical supersaturation, is required. All particles that are exposed to a supersaturation that is greater than the critical supersaturation grow to a critical diameter before reaching a state of instability where they grow indefinitely, or become activated.

Using the ASD, Köhler Theory-based relationships can be used to predict the CCN number concentrations assuming that the environmental aerosol contains some known fraction of a soluble organic or inorganic compound. If the size distribution and chemical composition of the ambient particles are simultaneously measured, then the

measured CCN behavior can be compared to that predicted by Köhler Theory on the basis of their size and composition (Seinfeld and Pandis, 1998). Conversely, Köhler Theory can be used to predict CCN concentration for a known aerosol of known composition. In this analysis, ammonium sulfate is assumed to represent the soluble component of aerosol with dry sizes smaller than 0.5 μm and sodium chloride for aerosol larger than 0.5 μm. The measured size distribution is used to predict the CCN number concentration at a series of fixed supersaturations between 0.1 and 1.0% and a soluble fraction between 0.1 and 1.0.

In addition, cumulative number concentration at each size bin of the ASD was calculated. This was used as a lookup table to relate the CCN number concentration and the cloud droplet concentration at cloud base to the Köhler Theory predictions of the minimum dry diameter activated (d_{pm}) based on assumptions of soluble fraction and uniform chemical composition (internally mixed). The CCN data were also fitted with the Twomey power-law dependence of total activated CCN number concentration (N_{CCN}) at a given supersaturation (s) of water vapor over cloud droplets $N_{CCN} = Cs^k$ (Twomey, 1959). This is done to calculate CCN concentrations at other supersaturations than the one measured. The CCN data are presented as shown in Figure 14. The averaged spectra and the standard deviation are based on measurements made below cloud base. The CCN averaging time is approximately equal to the time of the ASDs.

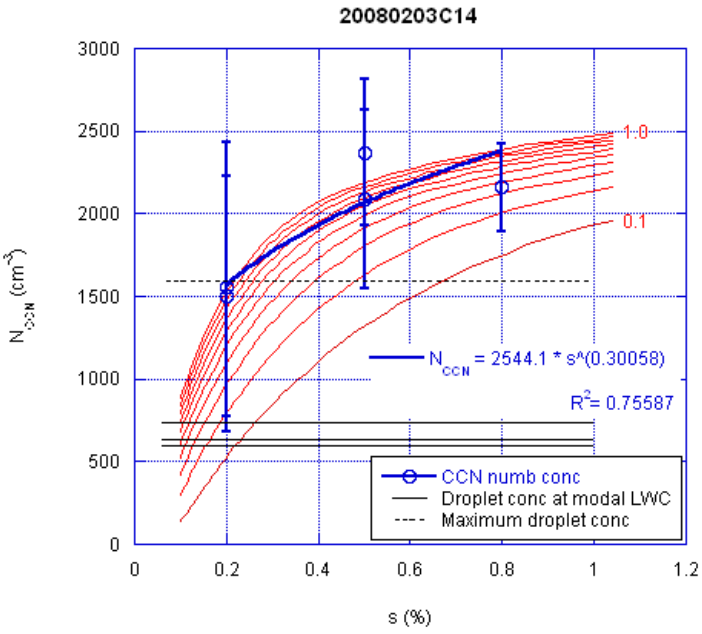

Figure 14. CCN spectra (blue circles) and Köhler Theory predictions of CCN (red trace) for 20080203 in Istanbul. The maximum droplet concentration and droplet concentration at modal LWC at cloud base are shown as absolute values on the left side of the graph.

5. DATA ANALYSIS PROCEDURE: CLOUD DROPLET EFFECTIVE DIAMETER AND CLOUD DROPLET CONCENTRATION

The cloud droplet effective radius (r_e) is often used as a representative parameter for the droplet size spectra. The r_e is defined as the ratio of the third to the second moment of the size spectrum and calculated from the CDP and FSSP size bin data; that is,

$$r_e = \frac{\int_{r=0}^{\infty} N_r r^3 dr}{\int_{r=0}^{\infty} N_r r^2 dr} \qquad \text{Eq. 2}$$

where r is the middle value for that size bin and N_r the droplet concentration in that size bin.

Previous studies have shown that clouds in polluted regions tend to have smaller r_e compared to similar clouds in cleaner environments (e.g., Kaufman and Fraser, 1997; Rosenfeld and Lensky, 1998 and Rosenfeld, 2000). It is also known that r_e below the precipitation forming level increases with cloud depth. As the cloud droplets rise to colder temperatures higher in the cloud, the excess water vapor can condense on them and they can also coalesce into larger droplets, both of which will increase r_e. Therefore it is important to separate the cloud depth effects from the aerosol load effects on r_e. Freud et al. (2008) report that for a given cloud depth, the cleaner the environment the larger are the effective radii.

A more comprehensive description of cloud microphysics must include the effects of entrainment mixing. Entrainment alters droplet concentrations, size distribution, cloud liquid water content (LWC), and cloud thermodynamics via complex and unresolved mechanisms. Precipitation efficiency is very sensitive to both cloud drop concentration and the shape of the size distribution; thus it will be useful to investigate the apparent relationships between aerosol and r_e at a known adiabatic fraction or adiabaticity (α). Adiabaticity is defined as

$$\alpha = \frac{LWC}{LWC_a} \qquad \text{Eq. 3}$$

where LWC is the liquid water content and the subscript "a" refers to the adiabatic value. LWC_a is assumed to be the upper limit of the LWC, because drier air is constantly entrained and then saturated at the expense of the already condensed water. Also precipitation and freezing of drops may reduce the LWC. Aircraft observations indicate that the ratio of observed to adiabatic LWC decreases with height above cloud base. Although the adiabatic LWC is always increasing with height, the actual LWC can decrease because the ratio of LWC to LWC_a decreases with the height above the cloud base. Karstens et al. (1994) parameterize the LWC_a value to account for the LWC reduction caused by entrainment, precipitation and freezing. This expression is given in Eq. 4.

$$LWC_p = LWC_a(1.239 - 0.145\ln\Delta h) \qquad \text{Eq. 4}$$

where LWC_p is the parameterized LWC in gm^{-3} and Δh is the height above cloud base in m. LWC_a modified in such a way was found to give a realistic description of the vertical distribution of cloud water. In this analysis the expression in Equation 4 does not hold for each cloud. The constants in the equation are varied for each case so that the LWC_p is fit to the measured LWC profile of the clouds.

The primary instruments used for the analysis of the cloud data were the CDP and FSSP-100. By using the droplet spectra derived from the Mie scattering curve, the r_e, the LWC, and other parameters that describe the droplet size spectra have been calculated. In this study cloudy areas were defined using the CDP and FSSP threshold of total cloud droplet number concentration (CDNC) > 20 cm^{-3} and a LWC > 0.01 gm^{-3}. Ensemble-averaged cloud properties are presented in altitude sections of 100 m by calculating the mean value of cloud properties (e.g., CDNC, r_e, LWC, updraft, DSD). A range of adiabatic LWC values have been determined separately for each cloud based on variability in lifting condensation level computed from sub-cloud measurements of pressure, water vapor mixing ratio, and potential temperature and by assuming a moist adiabatic ascent through the cloud.

The first step in the analysis of the cloud penetrations was to identify the time that each cloud was sampled. Since most of the clouds studied here are convective, each cloud penetration was less than a minute in duration. Data from the CDP, FSSP and AIMMS were processed and checked for data quality. The data set was reduced by binning the cloud data into 100m intervals starting at cloud base. Mean values were then calculated for each 100m bin. Labview plots from the processing code are shown in Figure 15 to 18. Figure 18 shows the DSD for each second during a cloud penetration.

This DSD data was used to determine the data quality of the bin size distribution of the CDP.

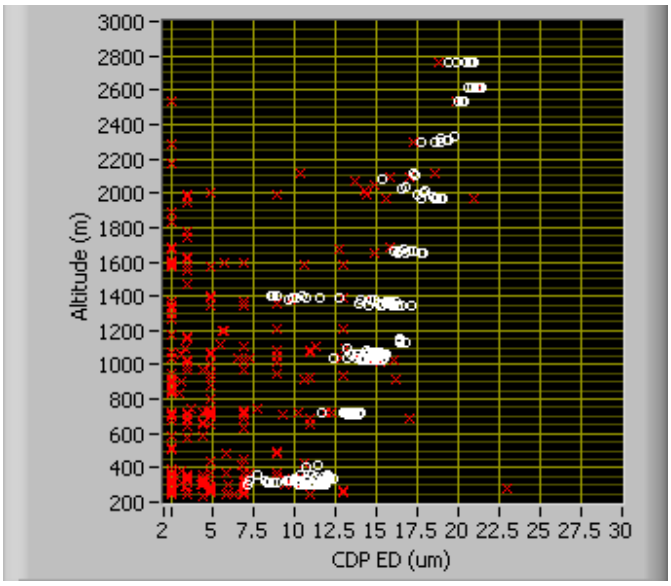

Figure 15. Effective diameter (μm) vs. cloud depth (m) for a convective cloud measured on 20040902 in West Texas (cloud C6). The white dots indicate accepted values when the CDNC > 20 cm^{-3} and LWC > 0.01 g m^{-3}. Red crosses are rejected data.

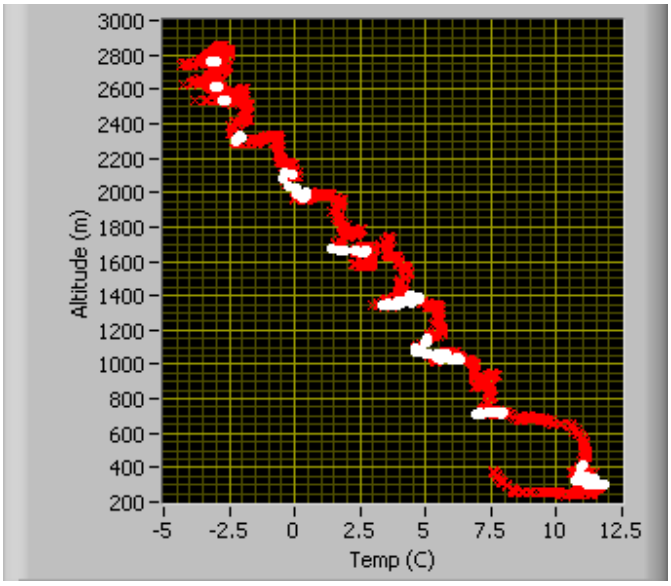

Figure 16. Same as Figure 15 but for temperature (°C).

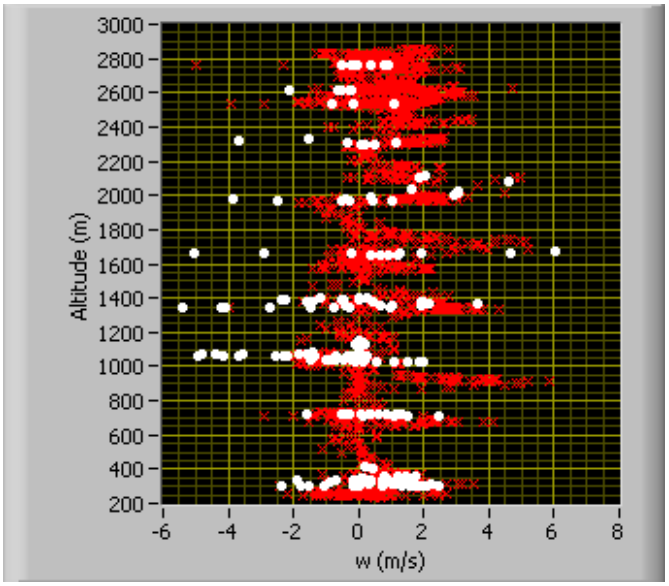

Figure 17. Same as Figure 15 but for vertical velocity (ms^{-1}). Negative values are updraft and positive values are downdraft.

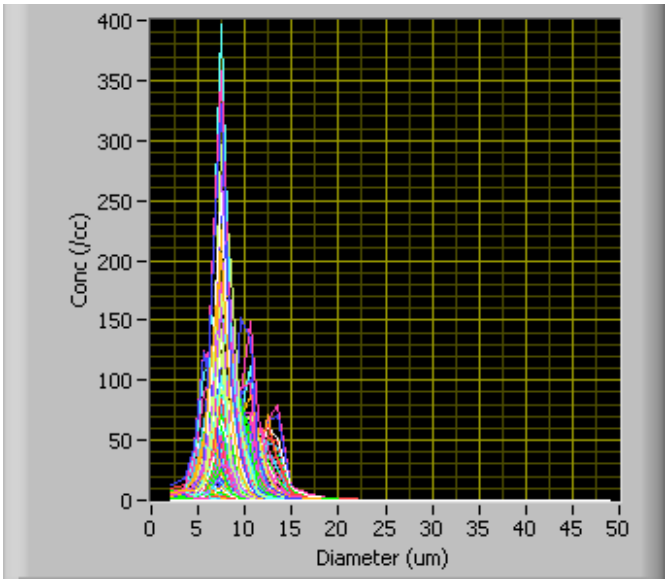

Figure 18. Cloud droplet size distribution (dN/dlogD, cm^{-3}) for 1Hz cloud penetration data.

The second step was to further reduce the data by rejecting cloud droplets that may be affected by dry-air entrainment, activation of entrained particles and mixing. This was done by diluting the LWC_a and adjusting the constants in Equation 4 to fit the measured LWC profile. The LWC_p profile was divided by a constant of 4. Any droplets with measured LWC less than 0.25 LWC_p were rejected. Finally, the mean was calculated for r_e values with LWC above the 85^{th} percentile. Labview plots describing this analysis are shown in Figure 19 and 20. Notice that in Figure 15 entrained droplets are measured at effective diameters ranging from 8 to 12.5 μm at a cloud depth of 1.4 km. These effective radii are equal to that measured at cloud base. The aircraft also measured the highest updraft of 5.4 ms^{-1} at 1.4km. This suggests that aerosols entrained in the updraft are activated at a higher supersaturation than that present at cloud base and could have an effect on the linearity of the effective radius profile in convective clouds.

The processing code described above rejects these entrained droplets during the second step of data processing as shown in Figure 20.

The analysis of the cloud penetration data focuses on the relations between r_e and cloud depth in the various aerosol regimes. The results are described in the next section.

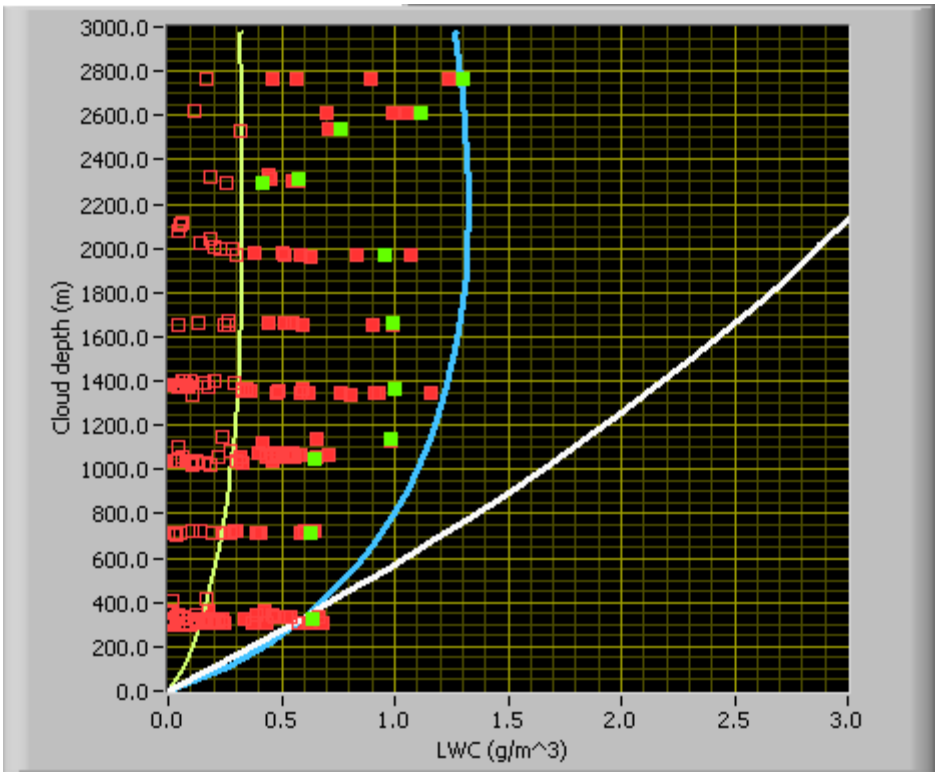

Figure 19. LWC (g m^{-3}) vs. cloud depth (m) profile binned at 100m intervals for 20040902C6. The red squares are the 1Hz LWC measurements. The filled squares have been accepted for analysis while the hollow squares are rejected. The white trace is LWC_a. The blue trace is the parameterized LWC profile LWC_p and the yellow trace is equal to 0.25 LWC_p. LWC data smaller than 0.25 LWC_p are rejected. The green squares are mean values for accepted LWC data above the 85th percentile.

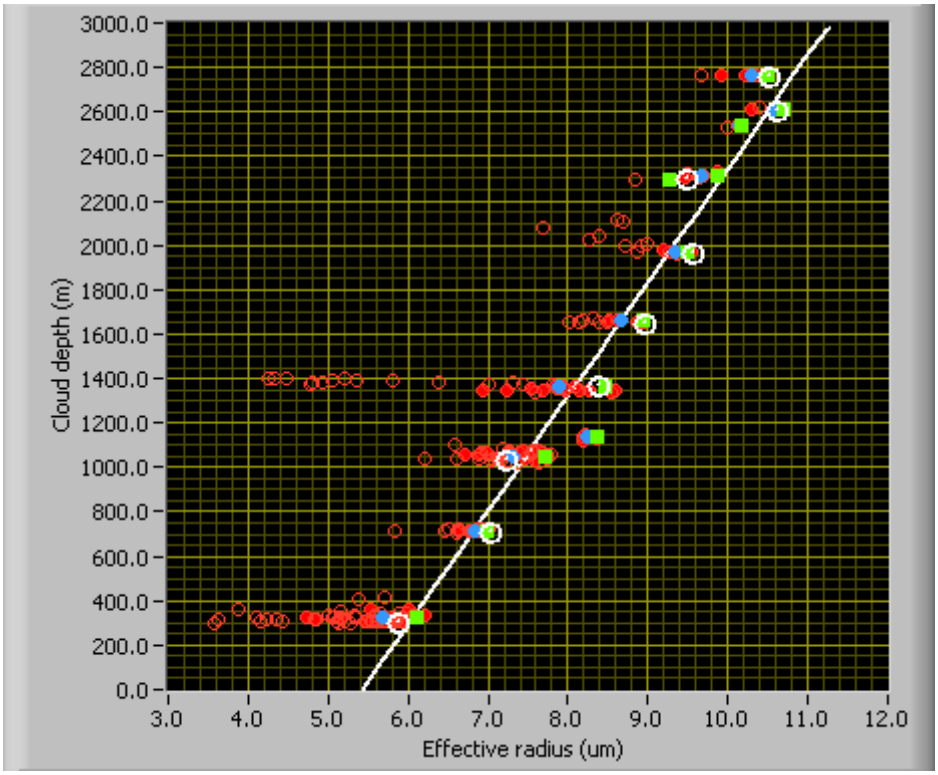

Figure 20. Same as in Figure 19 but for r_e. Blue circles are the mean r_e for all accepted droplets. The green squares are mean r_e values for accepted droplets above the 85th percentile. White circles are the mean r_e for accepted droplets that correspond to LWC above the 85th percentile. The white line is a bisquare linear fit.

6. RESULTS

Results from data analysis of 24 pairs of sub-cloud aerosol and cloud penetration data are presented in this section. Measurements of fine and coarse mode aerosol concentrations from the DMA, PCASP, CDP and FSSP instruments were combined and fitted with lognormal distributions. The fit parameters of the lognormal distributions are compared with cloud droplet effective radii retrieved from 260 cloud penetrations. Seventy six cloud penetrations were done in West Texas in August and September of 2004, 38 penetrations were done in central Saudi Arabia in April 2007 and 149 penetrations were done in Istanbul from February through June of 2008.

The first objective of this study is to identify typical aerosol size distributions at cloud base and to characterize the variability of the size distribution. The large variability in aerosol loading can be defined by the parameters that describe the 4 modes of the combined ASD. The modes represent multiple independent populations of aerosols. As mentioned in section 3, each mode is defined by the total number concentration N (cm^{-3}), the geometric standard deviation σ_g, and the geometric mean diameter D_g (μm). An increase or decrease in the magnitude of N directly affects the number of aerosols available to become cloud droplets. The values of D_g determine the position of the mode in the ASD. Increasing or decreasing D_g changes the number of activated aerosol, or CCN, as D_g approaches the minimum dry diameter (d_{pm}), the smallest dry diameter that will activate at a given supersaturation. More specifically σ_g affects the shape of the ASD. Increasing σ_g widens and flattens the lognormal fit while

decreasing σ_g narrows the fit. The parameters of each of these modes are given in Table 4.

Plots of the mode parameters can display the systematic characteristics of the size distributions. Quick inspection of Figures 21 to 23 reveals that the ASDs for each region have distinct features. The Texas ASDs are characterized by a high nucleation mode while ASDs in Riyadh are observed to have a high coarse mode. The ASDs in Istanbul exhibit a high nucleation mode. To examine the particle diameters of the modes, the mode number concentration is plotted vs. mode diameter for all 3 projects. This is shown

Table 4. Fit parameters for all ASDs in this study with information on total number concentration N (cm^{-3}), geometric mean diameter D_g (μm) and geometric standard deviation σ_g. The numbers 1 to 4 indicate the different modes.

Date	N 1	N 2	N 3	N 4	D_g 1	D_g 2	D_g 3	D_g 4	σ_g 1	σ_g 2	σ_g 3	σ_g 4
20040826C1	12800	3214.93	578.59	0.4	0.0086	0.022	0.1	1.1	1.55	1.8	1.63	1.8
20040827C2	11400	1163.01	379.44	8	0.0076	0.048	0.15	0.92	1.78	1.65	1.6	1.73
20040827C3	11400	1163.01	379.44	8	0.0076	0.048	0.15	0.92	1.78	1.65	1.6	1.73
20040828C4	1850	1008.66	256.81	3.5	0.0084	0.044	0.14	0.75	1.6	1.9	1.6	2
20040902C5	1233.37	582.87	775.85	0.17	0.009	0.04	0.12	1.88	1.57	1.97	1.66	1.52
20040902C6	1233.37	582.87	775.85	0.17	0.009	0.04	0.12	1.88	1.57	1.97	1.66	1.52
20040904C7	9900	1103.61	351.74	0.12	0.0086	0.039	0.17	1.9	1.65	1.8	1.63	1.4
20040905C8	6189.04	735	601.27	0.22	0.0084	0.034	0.12	1.4	1.69	1.46	1.64	1.5
20070405C9	936.49	953.16	30	33.32	0.027	0.073	0.57	1.27	1.75	1.8	1.6	1.95
20070407C10	74.4	140.08	22.83	8.97	0.022	0.086	0.5	2.56	1.66	1.76	2.53	2.05
20070408C11	141.07	140.23	19.68	11.23	0.026	0.091	0.48	1.37	1.85	1.8	1.8	2.33
20070409C12	432	35	28.52	6.71	0.1	0.87	2.25	7	2.05	1.5	1.33	1.66
20070411C13	137.71	20	6.9	1.41	0.087	0.63	2.17	4.24	1.96	1.7	1.38	1.7
20080203C14	500.03	1347.7	663.89	2.49	0.028	0.087	0.2	1.14	1.5	1.55	1.5	2.25
20080204C15	464.71	1355.37	566.12	1.87	0.028	0.099	0.2	0.9	1.5	1.69	1.52	2.62
20080319C16	2375	460	515.69	1.4	0.024	0.07	0.18	1.9	1.5	1.45	1.48	2
20080404C17	17.15	834.29	764.94	0.7	0.019	0.092	0.21	2.15	1.5	1.58	1.52	2
20080405C18	4509.7	1711.83	330.57	0.35	0.016	0.051	0.19	1.9	1.6	1.8	1.56	2
20080416C19	5340.34	298.53	334.47	0.28	0.018	0.046	0.11	2	1.41	1.48	1.62	2
20080416C20	3738.14	167.94	385.5	1.16	0.026	0.07	0.15	1.38	1.45	1.28	1.51	2.2
20080606C21	44.77	381.65	489.54	2	0.015	0.053	0.16	1.4	1.5	1.55	1.64	2.2
20080606C22	44.77	381.65	489.54	2	0.015	0.053	0.16	1.4	1.5	1.55	1.64	2.2

Table 4 Continued

Date	N 1	N 2	N 3	N 4	D_g 1	D_g 2	D_g 3	D_g 4	σ_g 1	σ_g 2	σ_g 3	σ_g 4
20080607C23	311.58	185.88	206.35	0.79	0.056	0.11	0.22	1.58	1.5	1.41	1.5	1.8
20080607C24	510.65	283.31	82.36	0.83	0.067	0.18	0.31	1.3	1.75	1.42	1.26	2.05

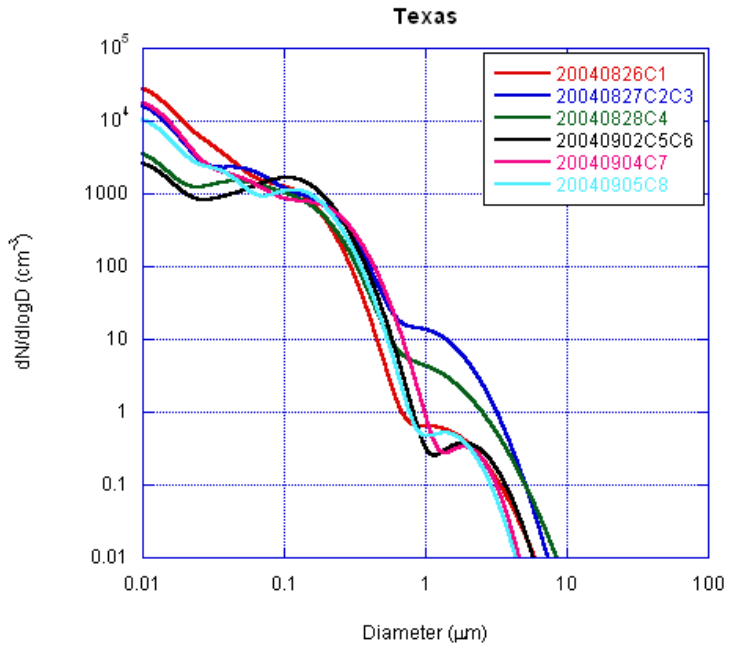

Figure 21. ASD for measurements in the vicinity of clouds in Texas.

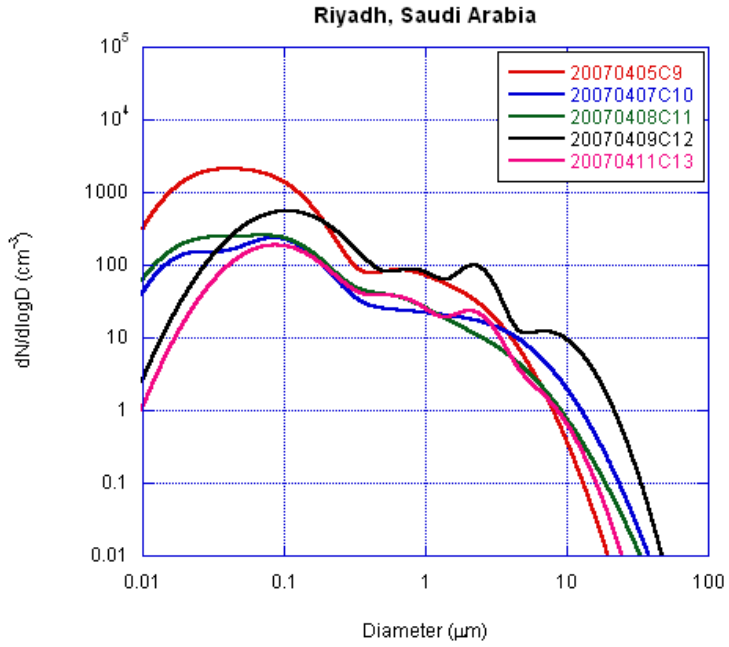

Figure 22. Same as Figure 21 but in Riyadh, Saudi Arabia.

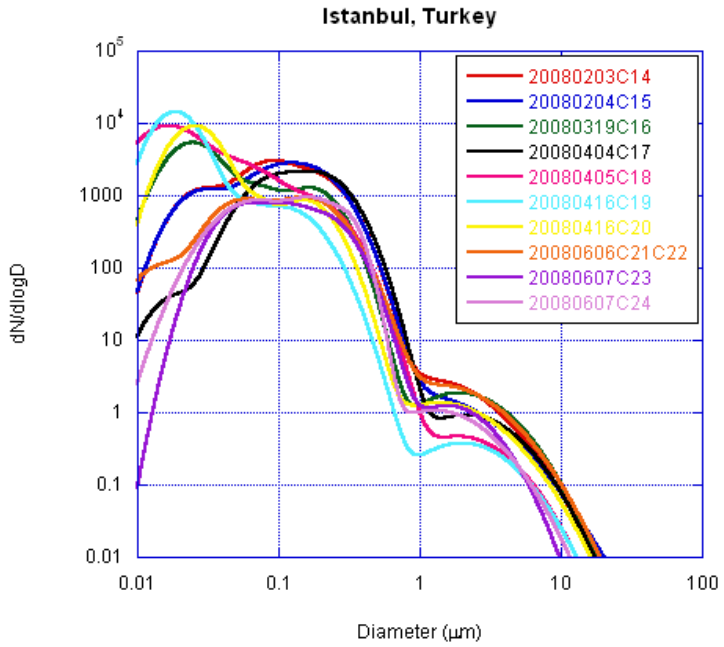

Figure 23. Same as Figure 21 but in Istanbul, Turkey.

in Figure 24. The nucleation mode is characterized by Mode 1. Clustering of high nucleation mode particles from Texas is evident with concentrations ranging from 1233 to 12800 cm^{-3} at an average diameter of 0.0084 µm. The cluster of concentrations > 5000 cm^{-3} is associated with southwesterly backtrajectories while the lowest concentrations on 20040902 are associated with easterly trajectories. The nucleation mode concentrations in Riyadh are low (< 1000 cm^{-3}) with an average mode diameter of 0.052 µm. Istanbul ASDs have the most variable nucleation mode with mode concentrations varying 2 orders of magnitude from a minimum of 45 on 20080606 to a maximum of 5340 on 20080416. The ASD measurements were made at a similar altitude of about 1km and at the approximate same location (see Figure 6 for C19 and C21). The nucleation mode fits for both cases had a similar mode diameter and standard deviation (see Table 4). In the

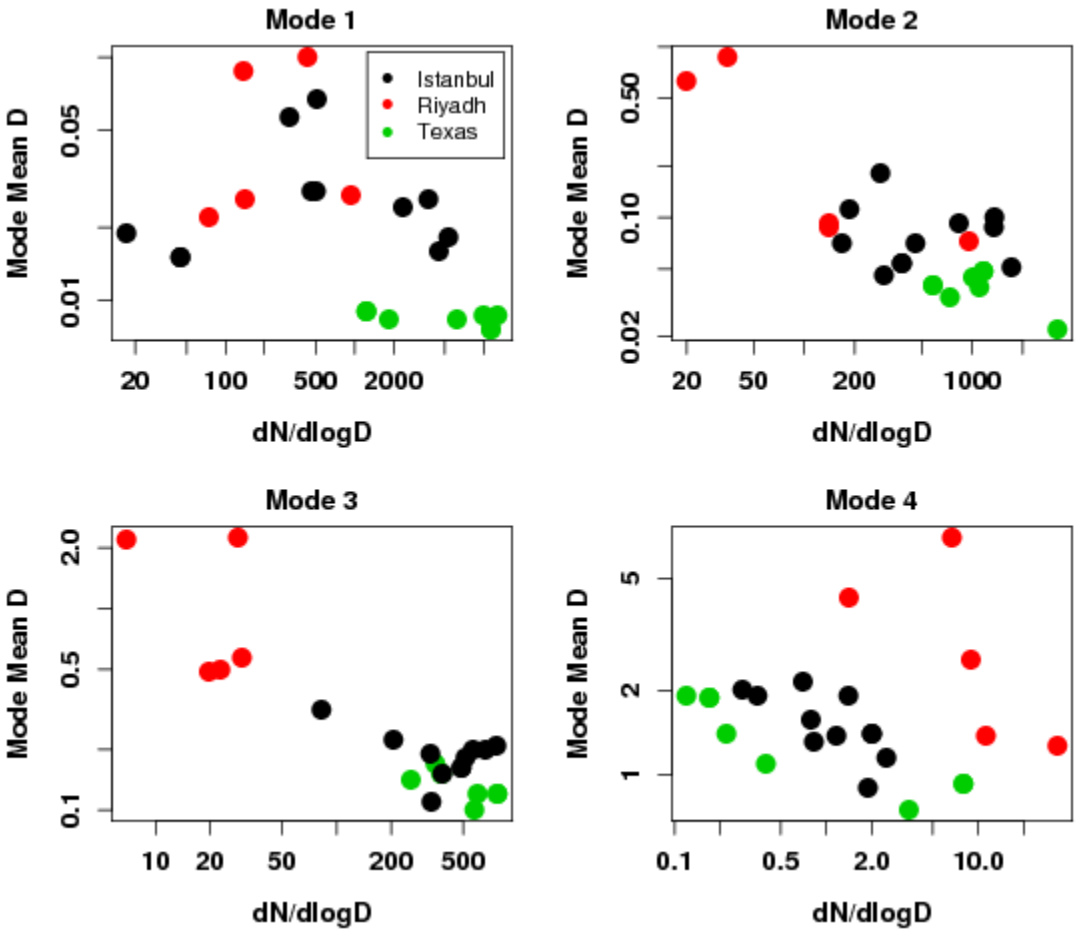

Figure 24. Comparison of mode mean diameter and mode concentration for all projects.

20080416 case the backtrajectories originated from Southwestern Europe while in the 20080606 case northerly flow from the Ukraine and Black Sea is indicative of pre-frontal conditions.

In most cases the Aitken mode and accumulation mode are characterized by mode 2 and 3 respectively. Common features can be identified in these modes. Texas ASDs

20080416 case the backtrajectories originated from Southwestern Europe while in the

20080606 case northerly flow from the Ukraine and Black Sea is indicative of pre-frontal conditions.

In most cases the Aitken mode and accumulation mode are characterized by mode 2 and 3 respectively. Common features can be identified in these modes. Texas ASDs tend to have the highest mode concentrations and smallest mode diameter. Riyadh ASDs have the smallest Aitken and accumulation modes with large mode diameters. Clustering is observed in the Istanbul ASDs in the accumulation mode with a mean concentration of 433 cm^{-3} and a mean diameter of 0.19 μm.

Riyadh shows distinctive signatures in mode 4. Mode 4 is characteristic of the coarse mode aerosol. Less clustering is apparent in this mode which accounts for the variability of coarse mode particles. Coarse mode particles are produced by processes of disruption of bulk material and re-suspension of sediment. In Riyadh dust was encountered on numerous research flights which provided opportunities to study dust-cloud interactions. Inspection of Figure 24 reveals that coarse mode concentrations in Riyadh exceed 6 cm^{-3} in all but one case. The case with the highest coarse mode occurred on 20080409 when a coarse mode of 33 cm^{-3} was measured. On this day a dust storm developed that reduced the visibility to less than a 100 m during the time the measurements were made.

The overall ASD depends on the contribution of particles produced by different mechanisms. Texas nucleation mode aerosols are often below 0.01 μm. Gas-to-particle conversion reactions are probably the major sources of this mode. Nucleation mode aerosol in Istanbul is highly variable with mode concentrations ranging over 2 orders of magnitude. It is thought that local pollution sources are responsible for the high

nucleation mode in Istanbul. Texas and Istanbul ASDs show a steep slope in the 0.4 to 0.5 µm range but this is conspicuously missing in Riyadh. Texas and Istanbul ASDs have a smaller standard deviation in the nucleation mode (see mode 3 in Figure 25 and 26) indicating that particles in the nucleation and Aitken mode grow to a narrow distribution. This suggests that a condensation mechanism is operative. Riyadh modes have high standard deviation where the modes combine and flatten the lognormal fit. In each of the Riyadh ASDs, the original structure of each mode is not apparent. This is

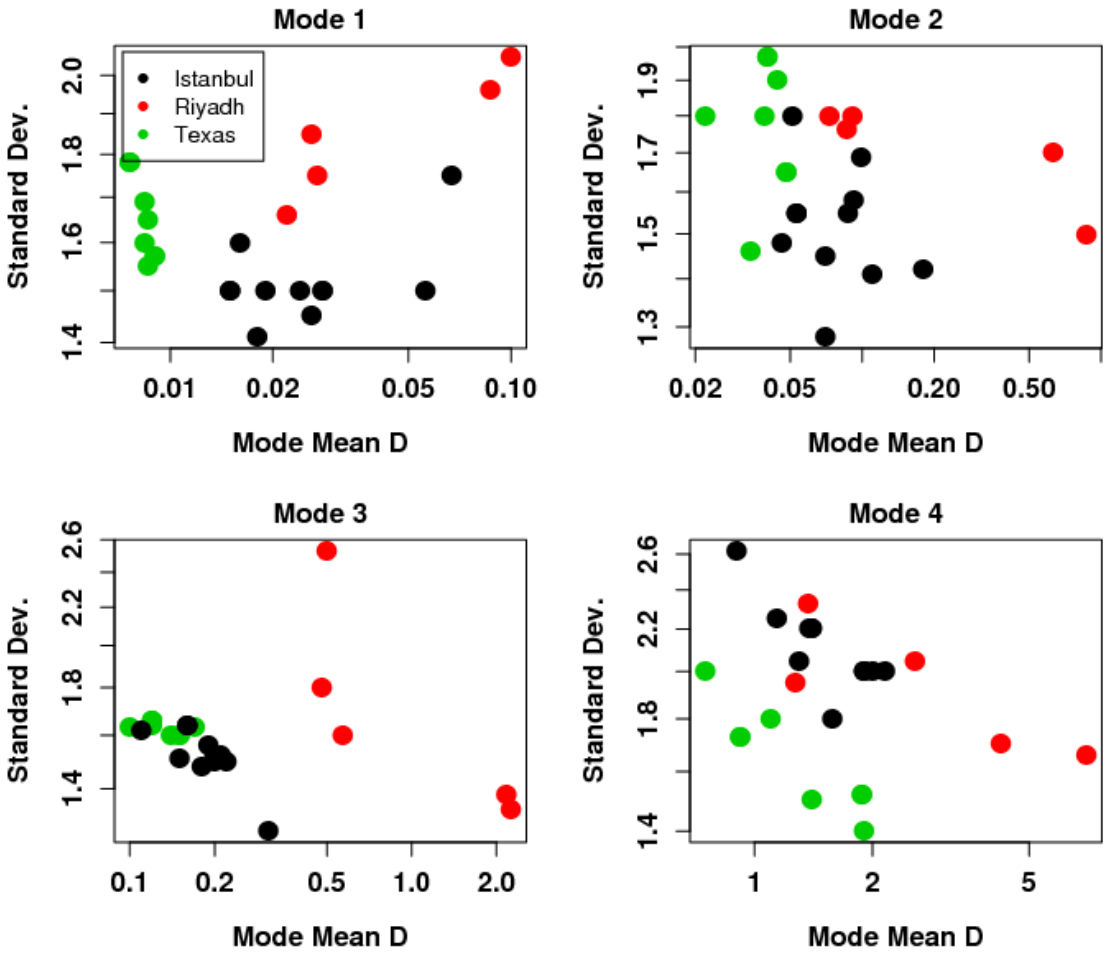

Figure 25. Comparison of mode mean diameter and standard deviation.

indicative of aged aerosol and intermodal coagulation including particles in adjacent modes. The coarse mode in Riyadh is primarily desert dust and is maintained by mechanical lifting and stratification. Trajectory analyses show that dusty conditions are caused by altitude-independent trajectories that originate in the Nubian Desert, southern Egypt and northern Sudan. This suggests that the particles in this layer are Saharan dust aerosols. Within this Saharan dust layer the coarse mode particle number concentration remained roughly constant at about 6 to 12 cm^{-3}.

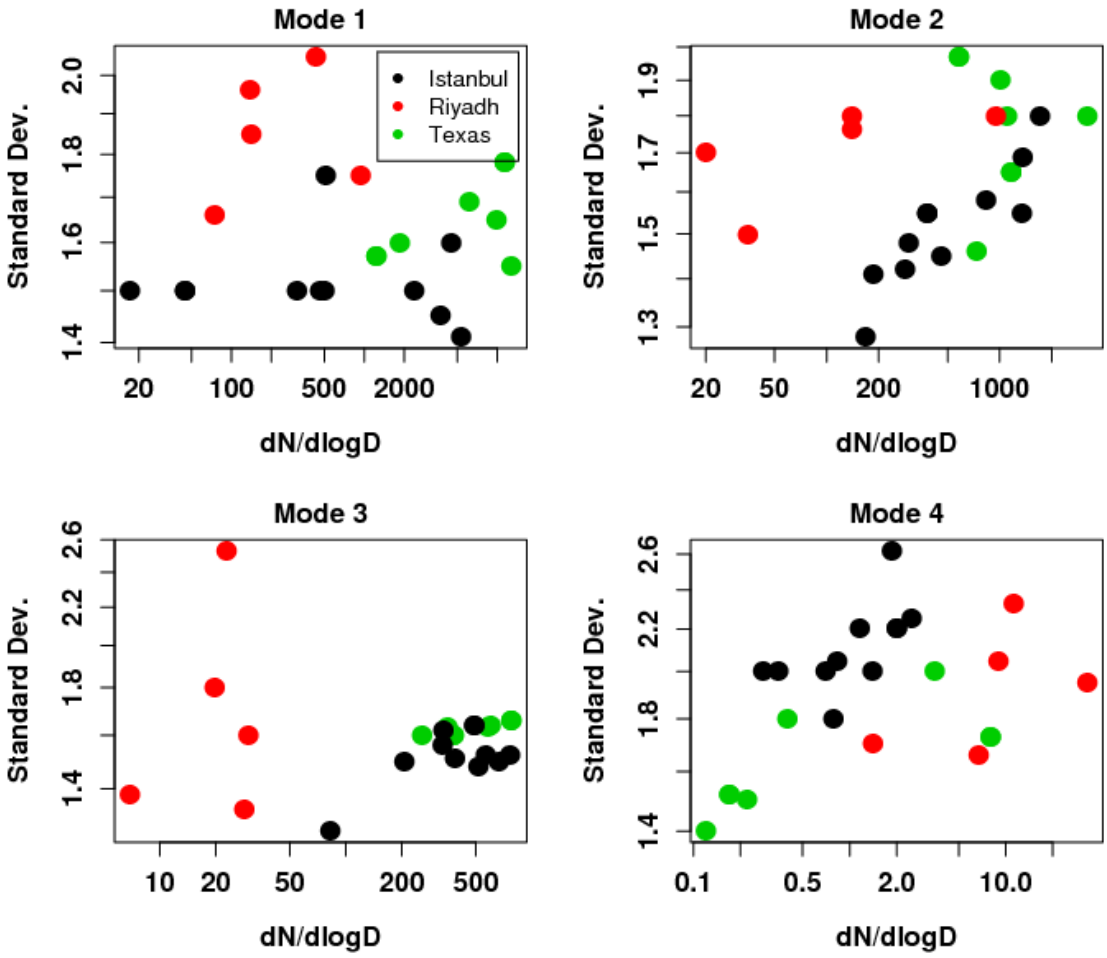

Figure 26. Comparison of mode concentration and standard deviation.

While the concentration and diameter of the nucleation mode is important in identifying new particle formation events, the position of the Aitken and accumulation mode are more important for determining the number of aerosols which become CCN. As the supersaturation increases, the number concentration of CCN increases gradually starting from the larger aerosols that activate at a small supersaturation to smaller aerosols that activate at a larger supersaturation. The modal analysis is a powerful tool in describing the structure of the ASD; however an attempt to relate the mode parameters to r_e was unsuccessful. To facilitate identification of cases analyzed here, each flight is identified by a letter as shown in Figure 27. Figure 28 and 29 show matrix plots that describe the mode diameter and number concentration when compared to the r_e at cloud base, 0.5 km, 1 km and 1.5 km. These figures are discussed in the figure captions. In general the relationships were observed to be weak and simplification of the data set was needed. The modal parameters that describe the 4 lognormals introduces 12 (4 X 3) variables for statistical relationships. In order to simplify the analysis, cumulative concentrations were calculated integrating from the largest size in the ASDs to cutoff dry diameters of 1.1, 0.1 and 0.06 µm. This data is shown in Table 5.

a	8/26/04	m	4/11/07
b	8/27/04	n	2/3/08
c	8/27/04	o	2/4/08
d	8/28/04	p	3/19/08
e	9/2/04	q	4/4/08
f	9/2/04	r	4/5/08
g	9/4/04	s	4/16/08
h	9/5/04	t	4/16/08
i	4/5/07	u	6/6/08
j	4/7/07	v	6/6/08
k	4/8/07	w	6/7/08
l	4/9/07	x	6/7/08

Figure 27. Letters a to x identifying cases in this study.

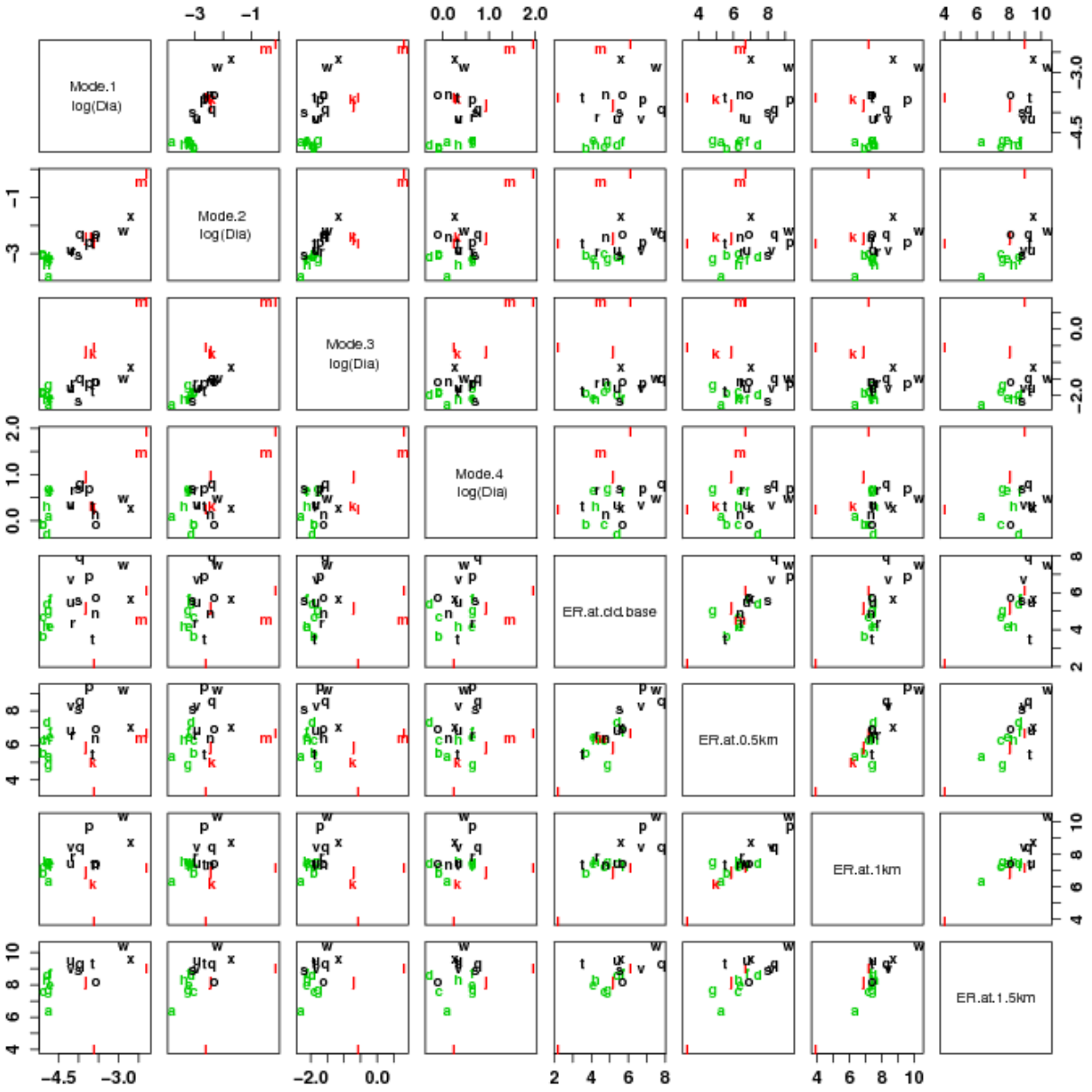

Figure 28. Matrix plot of mode mean diameter (Mode# log(Dia)) and effective radius (ER) at cloud base, 0.5 km, 1 km and 1.5 km. The effective radius measurements are retrieved from the nearest penetration above a fixed height. Diameter is in natural logarithm scale. No relationship is apparent between the position of the mode and the effective radius.

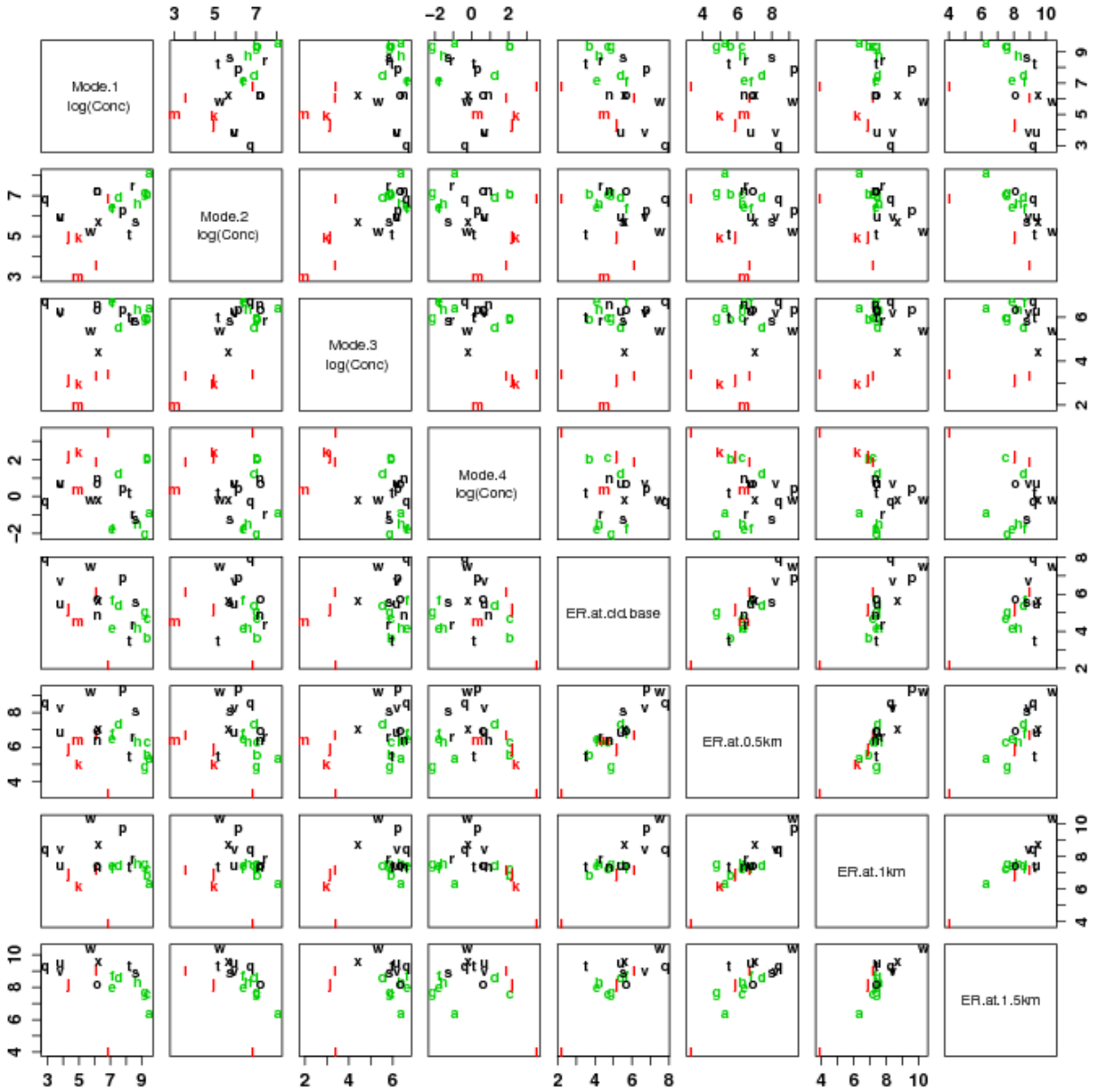

Figure 29. Same as in Figure 28 but for mode number concentrations (Mode# log(Conc)) in Texas. Mode concentration is in natural logarithm scale. No relationship is apparent between the mode number concentrations and the effective radius.

Table 5. Summary of aerosol and cloud measurements.

Date	Altitude for ASD (m)	ASD Integrated to 0.06 (μm)	ASD Integrated to 0.1 (μm)	ASD Integrated to 1.1 (μm)	Height at $r_e = 12\mu m$ h_{12} (m)	r_e at cloud base	r_e at 0.5km	r_e at 1km	r_e at 1.5km
20040826C1	1910	547.1	269.4	0.1	6219	-	5.3	6.3	6.3
20040827C2	1479	644.7	347.6	1.0	2198	3.7	5.6	6.9	-
20040827C3	1479	644.7	347.6	1.0	4538	4.7	6.25	7.2	7.5
20040828C4	1818	510.7	267.1	0.5	2890	5.4	7.4	7.5	8.6
20040902C5	1879	736.3	465.9	0.0	2709	4.1	6.4	7.4	7.9
20040902C6	1879	736.3	465.9	0.0	3484	5.7	6.8	7.3	8.7
20040904C7	1658	520.2	307.6	0.1	3428	4.9	4.8	7.4	7.6
20040905C8	2254	515.8	317.5	0.1	3131	4.2	6.3	7.6	8.3
20070405C9	2907	725.6	337.1	4.0	6744	2.2	3.3	3.9	4
20070407C10	4037	119.5	62.1	1.5	3126	5.2	5.9	6.9	8.1
20070408C11	3216	140.3	72.5	1.4	2502	-	5	6.2	-
20070409C12	3201	328.0	221.6	7.4	2273	6.1	6.7	7.2	9
20070411C13	3924	101.1	61.6	2.1	1419	4.5	6.4	-	-
20080203C14	923	1744.2	1120.5	0.5	2363	4.8	6.4	7.3	-
20080204C15	818	1664.9	1161.5	0.3	3057	5.7	6.9	7.4	8.1
20080319C16	1002	920.5	564.5	0.4	1302	6.8	9.3	9.6	-
20080404C17	916	1418.1	1071.2	0.2	4066	7.8	8.4	8.3	9.2
20080405C18	933	993.4	504.4	0.1	1986	4.3	6.5	7.8	-
20080416C19	906	374.6	209.0	0.1	2942	5.5	8	-	8.8
20080416C20	973	538.2	335.3	0.2	2916	3.5	5.5	7.4	9.3
20080606C21	1190	635.1	445.0	0.6	2258	5.4	6.8	7.4	9.4
20080606C22	1190	635.1	445.0	0.6	3673	6.7	8.2	8.4	8.9
20080607C23	1041	504.0	328.6	0.2	1898	7.5	9.2	10.3	10.4
20080607C24	856	644.8	456.4	0.2	3161	5.6	7	8.7	9.5

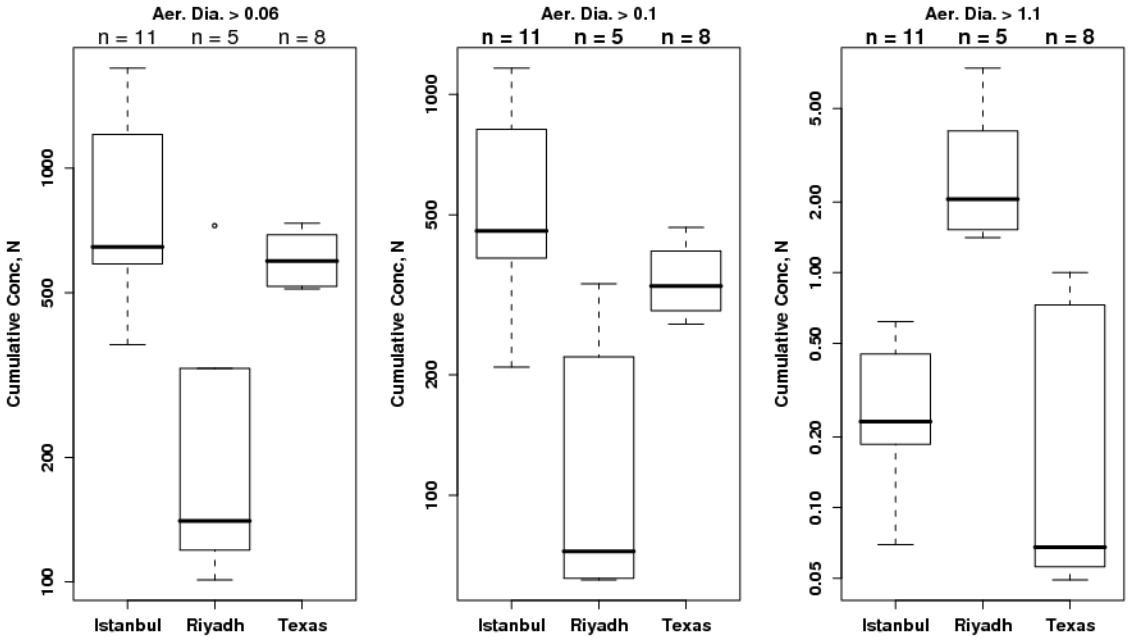

Figure 30. Box plots of the cumulative concentrations integrating from the largest size in the ASDs to cutoff dry diameters of 1.1, 0.1 and 0.06 µm. The data point for cumulative concentration > 1.1 µm from Riyadh that is greater than the 1.5 interquartile range above the 75th percentile is an outlier.

Cumulative concentrations represent the number concentration integrated to cutoff sizes. Figure 30 shows box plots of the cumulative concentrations. The data point for cumulative concentration > 1.1 µm from Riyadh that is greater than the 1.5 interquartile range above the 75th percentile is an outlier. This data point is from 20070405 when haze and dust were observed in Riyadh with aerosol optical thickness of 1.3 and visibility reduced to 6.5 km. On this day the Aitken mode was the highest amongst the Riyadh cases studied here. Cumulatively, the Istanbul ASDs are the most

polluted due to the high accumulation modes. The Texas ASDs show very little spread in cumulative concentration at cut sizes of 0.06 and 0.1 μm. This indicates that CCN concentrations are expected to have a small spread in the activation spectrum from one case to the other. The largest variability in CCN activation based on the ASD is expected in Riyadh due to the large spread in the cumulative concentrations > 0.1 μm. The Istanbul cumulative concentration plots show a large variability across each cut size suggesting that CCN concentrations would be highly variable for each of the cases studied here.

CCN data were analyzed for all the Istanbul cases except for C21 on 20080606 when the aircraft profiled 2 clouds (C21 and C22) and was unable to descend below the cloud bases of C21. The analysis of the CCN data is shown in Figure 31 and 32. The plots in these figures are used to estimate the soluble fraction of ammonium sulfate and sodium chloride. As mentioned earlier, ammonium sulfate is assumed to represent the soluble mass fraction of aerosol with dry sizes smaller than 0.5 μm and sodium chloride for aerosol larger than 0.5 μm. If the particle size and chemical composition were known, Köhler Theory could be used to calculate the supersaturation at which activation occurs. In this study the chemical composition was not measured. Therefore, the measured CCN spectrum is used to estimate the soluble fraction. This is done by comparing the measured CCN concentrations with the predicted CCN concentrations. For example, in the 20080203C14 case, the measured CCN at s=0.2%, 0.5% and 0.8% are 1556, 2088 and 2158 cm^{-3} respectively. By inspecting the $N_{CCN} = Cs^k$ fit and comparing the values of the measured CCN with the predicted CCN concentrations at solubility fraction varying from 0.1 to 1.0, a soluble fraction is chosen that best matches

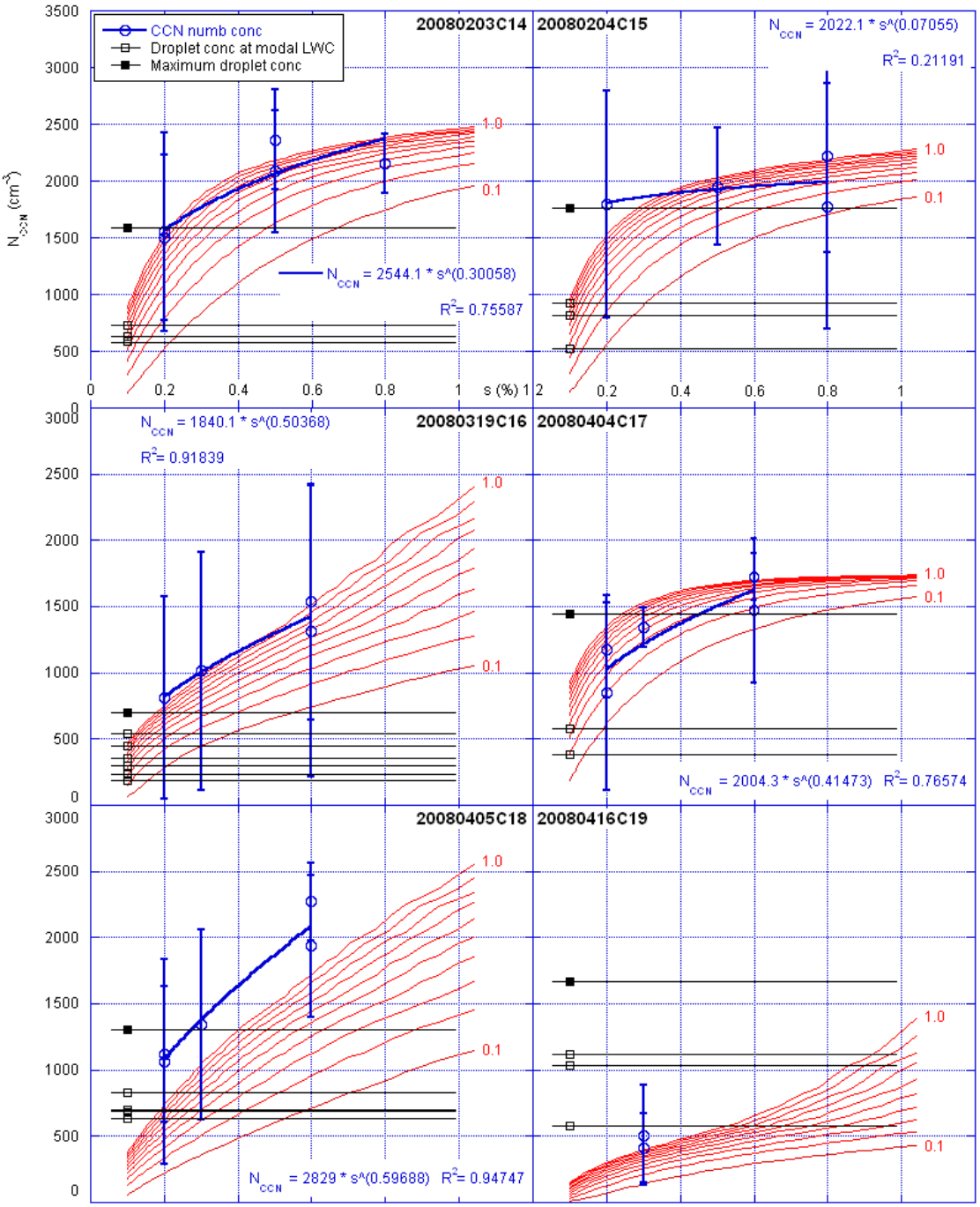

Figure 31. CCN spectra (blue circles) and Köhler Theory predictions of CCN (red trace) for Istanbul. The maximum droplet concentration and droplet concentration at modal LWC at cloud base are shown as lines across the graphs.

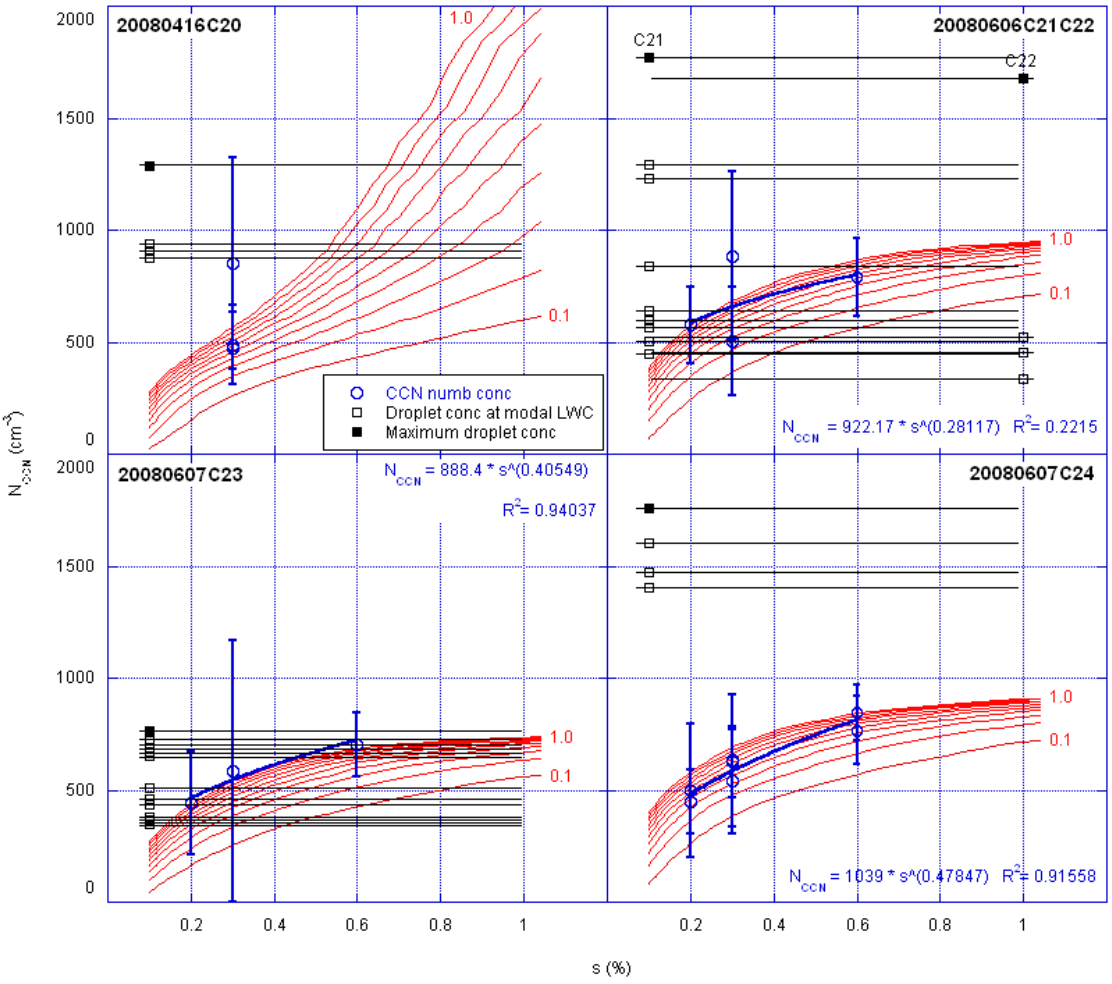

Figure 32. As in Figure 31 but for different cases.

the $N_{CCN} = Cs^k$ fit and the measured CCN spectrum. The assignments of soluble fraction ranged from 0.5 to 0.9. The minimum dry diameter activated (d_{pm}) at the specified supersaturation and assumed soluble fraction is also calculated. The results of this analysis are given in Table 6. On 20080203 and 20080204 the CCN measurements were made at 0.2%, 0.5% and 0.8% supersaturation. The $N_{CCN} = Cs^k$ equation for the power law fit was used to calculate the CCN concentrations at 0.2%, 0.3% and 0.6%. The

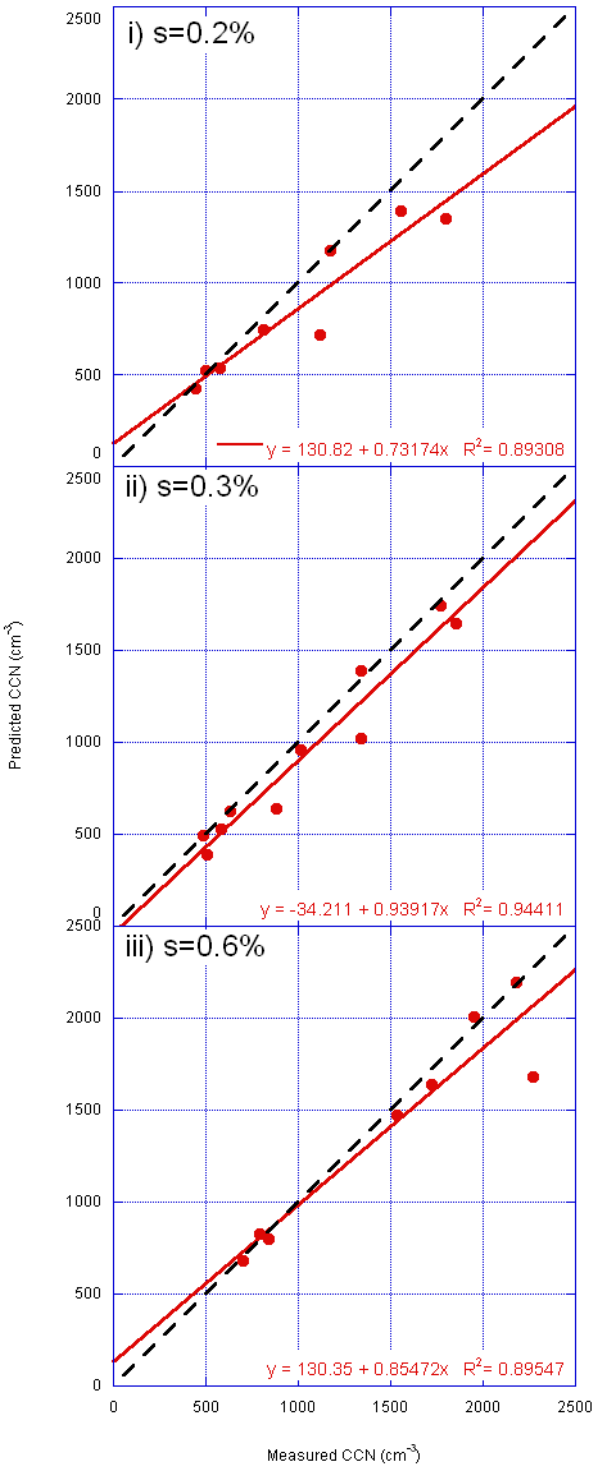

Figure 33. Correlation of the measured CCN concentration with the predicted CCN concentration using an assumed solubility fraction for each of the Istanbul cases.

correlation of the measured CCN concentration with the predicted CCN concentration using an assumed soluble fraction is shown in Figure 33. Data points tend to lie below the 1:1 line indicating that the predicted CCN concentrations are lower than the measured CCN concentrations. This can be confirmed by the inspection of Figures 31 and 32.

In order to investigate the sensitivities of the measured to predicted CCN correlation to the soluble fraction assumption, the predicted CCN concentrations were calculated for soluble fractions at +0.1 and -0.1 to that originally assumed. The mean percentage error for the cases in Table 6 is equal to ±3.7%. This means that if an incorrect assignment is made to the soluble fraction that equals ±0.1, the predicted CCN varies by ±3.7% at 0.3% supersaturation. The last column in Table 6 defines the origin of the airmass. Figure 34 shows the ASD as shown in Figure 23 but clustered according to backtrajectories.

Figure 35 shows the relationship between the ASD cumulative concentrations, the measured CCN concentration and the maximum cloud droplet concentration at cloud base for the Istanbul cases. It is worth noting that the cumulative concentration > 0.1 μm and > 0.06 μm show the expected relationship with the measured CCN at s=0.3%. An increase in the cumulative concentrations leads to an increase in the measured CCN. The relationship between the maximum droplet concentration at cloud base and CCN at 0.3% is evident for some of the cases. The outlying data points are cases C19, C21, C22 and C24. All the other cases seem to fall near a 1:1 line. A direct relationship between the cumulative aerosol concentrations and the maximum droplet concentration is not apparent.

Table 6. Measured CCN concentrations at s (CCN), assumed soluble fraction (SF), predicted CCN concentrations at s (PCCN) and minimum dry diameter activated at s (d_{pm}) are given. The measured CCN listed in bold are calculated using the $N_{CCN} = Cs^k$ fit. The percentage error in PCCN is calculated by assuming a SF of +0.1 and -0.1 to that originally assumed. (Air mass origin: C. Med – air mass backtrajectories from the Central Mediterranean with brief traverses over land; W. Med - air mass backtrajectories from the Western Mediterranean with long traverses over land; E. Eur - air mass backtrajectories from Eastern Europe and the Black sea with possible local influences.)

Date	CCN 0.2% (cm^{-3})	CCN 0.3% (cm^{-3})	CCN 0.6% (cm^{-3})	SF	PCCN 0.2% (cm^{-3})	PCCN 0.3% (cm^{-3})	PCCN 0.6% (cm^{-3})	% error in PCCN 0.3%	d_{pm} CCN 0.3% (μm)	d_{pm} PCCN 0.3% (μm)	Air mass origin
20080203C14	1556	**1772**	**2182**	0.7	1390	1744	2193	0.36	0.060	0.062	C. Med.
20080204C15	1798	**1857**	**1950**	0.6	1354	1649	2009	0.34	0.045	0.063	C. Med.
20080319C16	812	1014	1535	0.9	748	961	1471	0.34	0.055	0.058	W. Med.
20080404C17	1171	1344	1722	0.5	1177	1392	1640	0.37	0.070	0.065	E. Eur.
20080405C18	1120	1341	2270	0.9	722	1020	1679	0.47	0.047	0.060	W. Med.
20080416C19	-	507	-	0.9	-	390	-	0.37	0.045	0.059	W. Med.
20080416C20	-	488	-	0.6	-	490	-	0.50	0.068	0.068	W. Med.
20080606C21	-	-	-	-	-	-	-	0.32	-	-	
20080606C22	575	883	790	0.7	535	639	827	0.26	0.024	0.061	E. Eur.
20080607C23	443	583	704	0.9	430	531	678	0.37	0.048	0.057	E. Eur.
20080607C24	497	631	843	0.6	524	628	799	0.36	0.064	0.064	E. Eur.

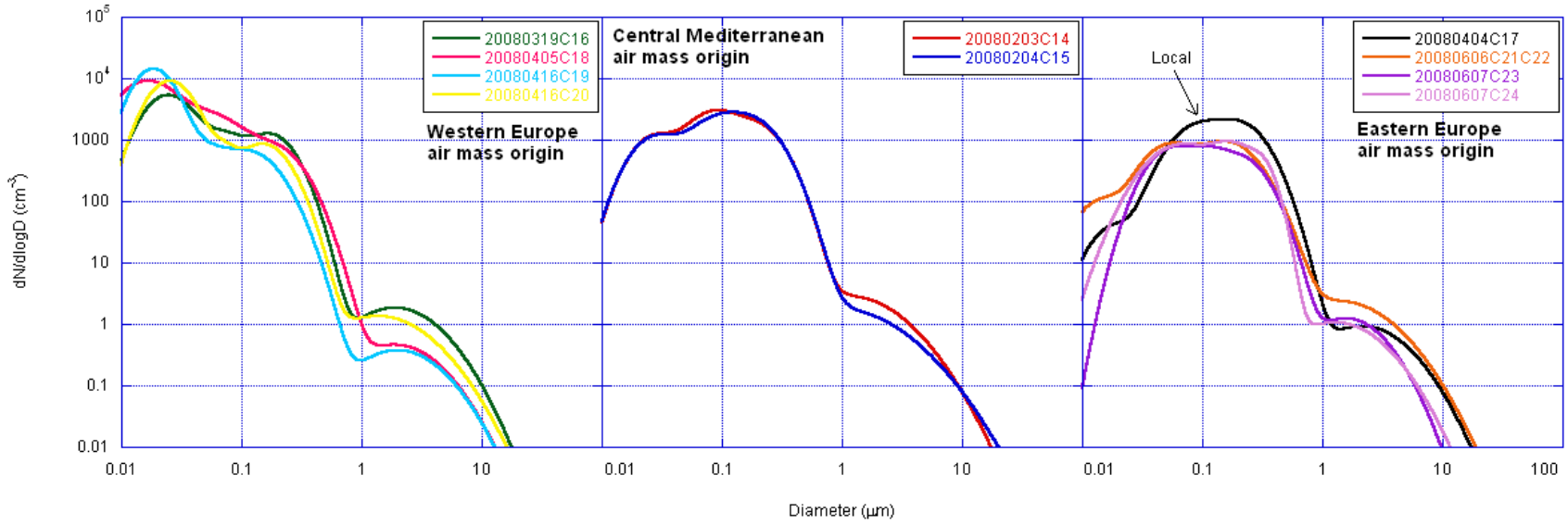

Figure 34. ASD as shown in Figure 23 but clustered according to backtrajectories. Airmasses that originate from Western Europe contain the highest nucleation and Aitken modes. Backtrajectories of Central Mediterranean origin contain a high accumulation mode but low nucleation mode. Eastern Europe backtrajectories have the lowest nucleation mode but exhibit a broad accumulation mode which is indicative of aging of well mixed urban aerosol.

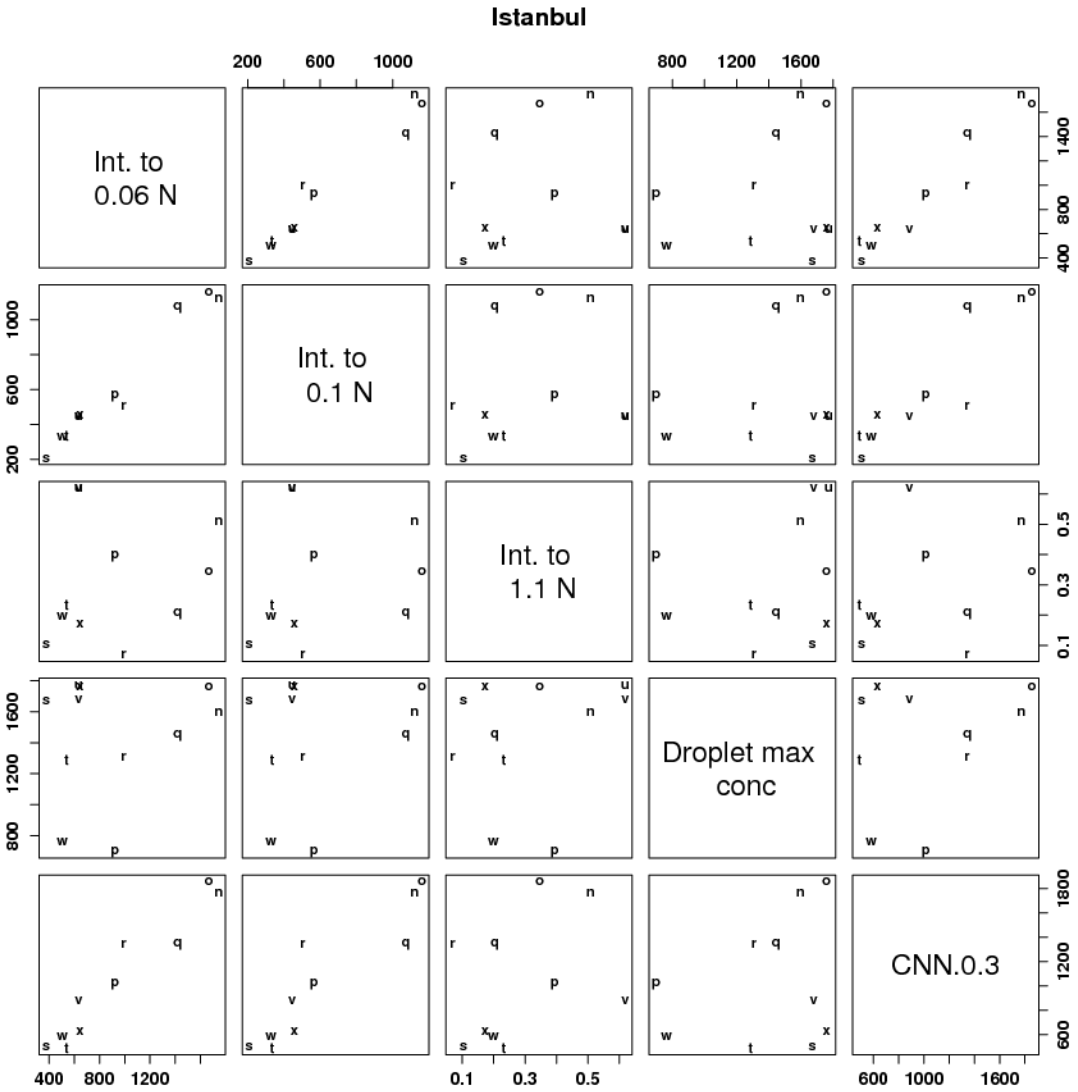

Figure 35. Matrix plot of cumulative concentration > 1.1 μm, > 0.1 μm and > 0.06 μm (cm^{-3}), maximum droplet concentration (cm^{-3}) at cloud base and measured CCN at s=0.3% (cm^{-3}).

The last objective of this study is to examine the relationship between the droplet effective radius and the height above cloud base in different aerosol regimes. Andreae et al. (2004) show how the DSD change with the vertical development of clouds. Although this is a comprehensive approach, it is difficult to employ this methodology for 3 different field campaigns especially since the cloud droplet spectrometers used on the aircraft are different. The CDP and FSSP DSDs have different properties. The FSSP is known to suffer from a coincidence problem where several smaller droplets are counted as one large one (Cooper, 1988). This problem can artificially widen the DSD and undercount smaller droplets. Freud et al. (2008) take a simpler approach by characterizing the DSD with a single parameter: the modal diameter of the DSD. This method was considered for this analysis but it was found to be more suitable for continental convective clouds where the DSD is characterized by a single narrow mode. In this study the choice of a single parameter has to be suitable for both extreme continental and continental convection. The r_e was chosen as a more robust parameter as it represents the spread of the DSD better. The processing code discussed in section 5 was developed to remove cloudy areas that may be affected by entrainment mixing, identify regions of high LWC and retrieve the r_e. The same retrieval procedure was used for all 3 projects and resulted in representative r_e values with small standard deviation. The r_e and the standard deviation were plotted with cloud depth as shown in Figure 36. The color of the best-fit line corresponds to the color of the ASDs shown in Figures 21 to 23. The vertical line at r_e of 12 μm corresponds to the modal diameter of the DSD for the onset of warm rain (Andreae et al., 2004). Since most of the linear fits exhibit strong R^2

values, the cloud depth at which r_e crosses the 12 μm threshold (h_{12}) is retrieved. These values are given in Table 7.

Table 7. Summary of analysis of cloud penetration data. Maximum droplet concentrations and LWC are for penetrations within 500 m of cloud base.

Date	Max drop conc > 2 μm (cm^{-3})	Max drop conc > 5.5 μm (cm^{-3})	Max drop conc at modal LWC (cm^{-3})	Modal LWC (cm^{-3})	h_{12} (m)	Maximum updraft (ms^{-1})
20080203C14	1595	1333	739	0.36	2363	3.4
20080204C15	1759	1526	921	0.48	3057	2.2
20080319C16	698	585	537	0.23	1302	1.4
20080404C17	1444	924	578	0.62	4066	5.7
20080405C18	1307	948	833	0.56	1986	1.6
20080416C19	1672	1454	1116	0.47	2942	1.6
20080416C20	1287	1104	938	0.43	2916	6.3
20080606C21	1773	1492	1290	0.33	2258	2.9
20080606C22	1679	1180	522	0.37	3673	5.3
20080607C23	764	567	721	0.92	1898	8.8
20080607C24	1759	1401	1758	0.86	3161	3.7

Figure 36 shows that only a fraction of the clouds reach the threshold of $r_e = 12$ μm. With no comparison data between the performance of the CDP in the Texas and Istanbul and between the CDP and FSSP, direct comparisons between r_e for each of the projects are avoided. Furthermore it is difficult to obtain accurately the cloud base height. The determination of cloud base is dependent on the observations of the flight scientist. Estimates of cloud base can be improved by flying the aircraft in the sub-cloud layer and climbing through the cloud base until visibility is reduced to less than 20 meters. An incorrect assignment of the cloud base height would introduce errors in the calculation of the LWC_a and hence LWC_p which is used to reject cloud droplets below a

threshold of adiabaticity. The parameter h_{12} should therefore be used cautiously as the data set is not sufficiently large to ignore these uncertainties. In addition, other variables such as updraft should not be ignored. Maximum updraft values from the Istanbul project ranged between 1.4 ms^{-1} on 20080319 to 8.8 ms^{-1} on 20080607. This variability suggests that the clouds sampled in Istanbul, although convective in nature, developed in different thermodynamic instability profiles from February through June 2008. The Texas clouds contained strong updrafts throughout the measurement period. The stronger updrafts cause higher supersaturations at cloud base which nucleate a larger fraction of the ASD. These droplets grow slower by diffusion and coalescence which would increase the value of h_{12}.

In this study h_{12} is used as a proxy for the slope of the r_e profile and to identify cases that do not reach the 12 μm threshold for warm rain. In Texas only 3 cases reach the 12 μm threshold at a cloud depth less than 3 km. These cases are 20040827C2, 20040828C4 and 20040902C5. The latter 2 cases have low nucleation modes while the first case has the highest coarse mode. In Saudi Arabia, 3 cases out of 5 have a value for h_{12} smaller than 3 km. Two of these cases, 20070409C12 and 20070411C12, have a conspicuously low nucleation mode. In addition, the 20070409C12 case was a dust storm and the r_e at cloud base is the largest of all the cases. In Istanbul 4 cases do not reach the 12 μm threshold at a cloud depth less than 3 km (20080204C15, 20080404C17, 20080606C22, 20080607C24). The high values of h_{12} in these 4 cases seem to be related to a high accumulation mode (and CCN) in C15 and C17 but $h_{12} > 3$ km for C22 and C24 cannot be explained.

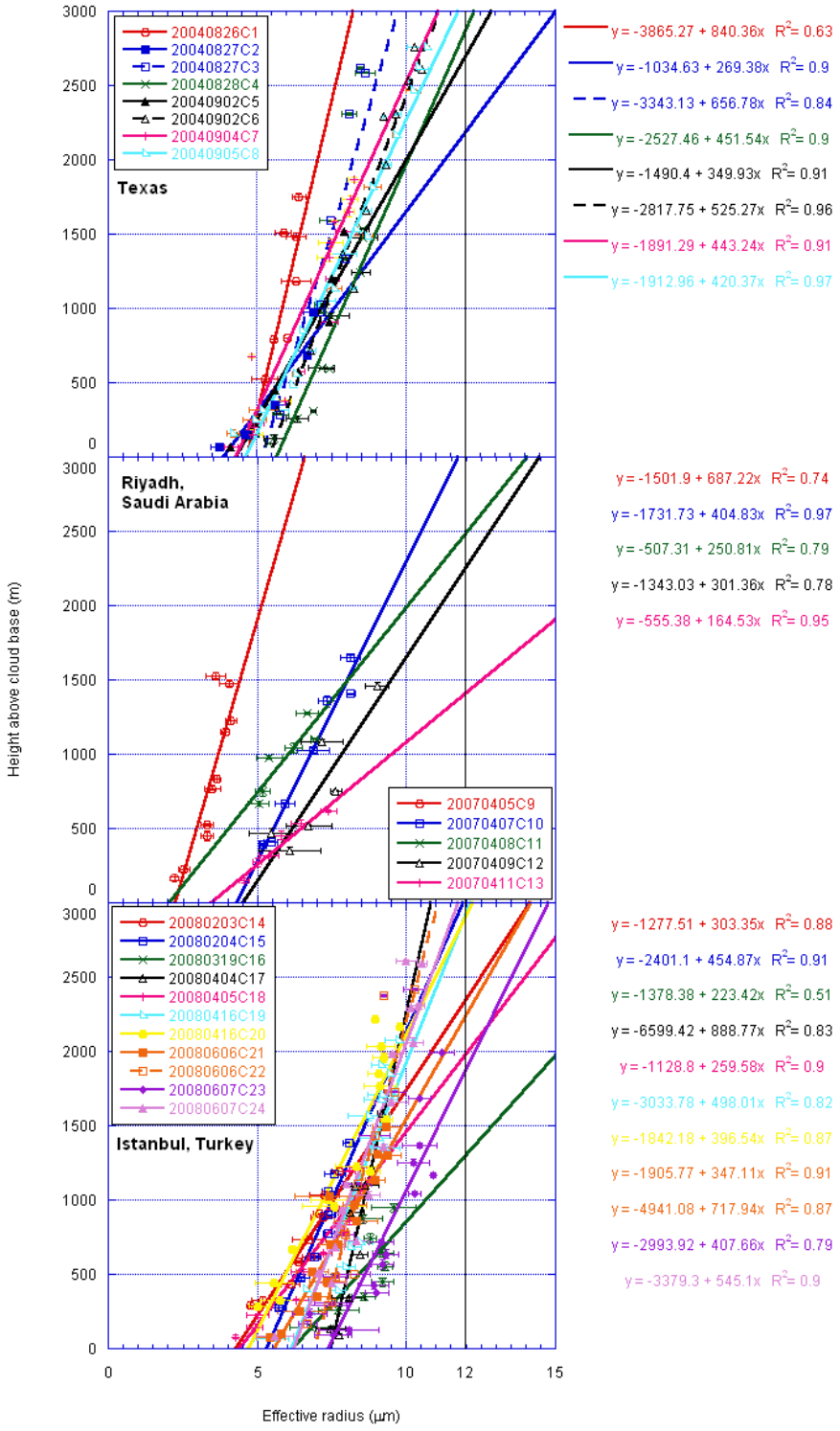

Figure 36. The growth of r_e with cloud depth for all cases. Each point represents the mean and standard deviations for r_e in a 100m height bin.

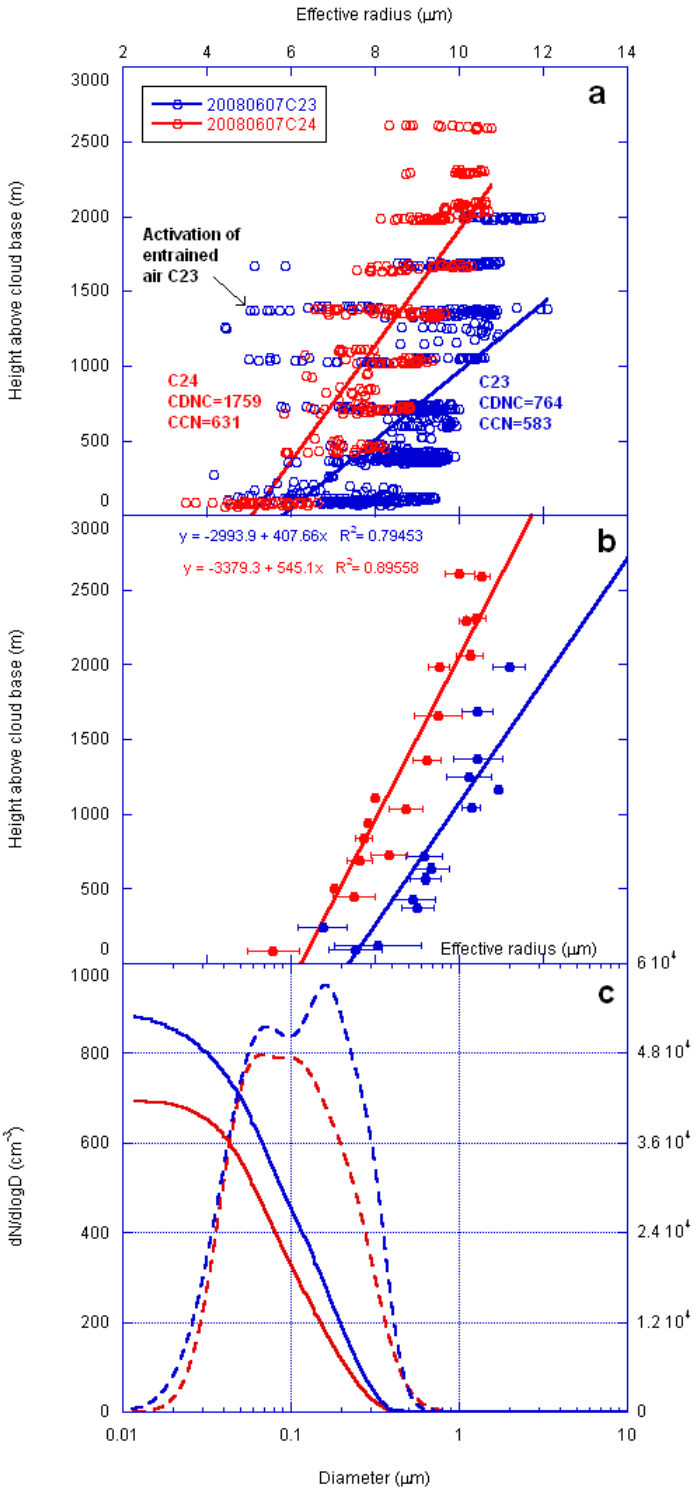

Figure 37. a) r_e profile CDNC > 20 cm^{-3} and LWC > 0.01 g m^{-3}; b) r_e profile processed; c) ASD (broken trace) and cumulative aerosol concentration (solid trace).

Of interest is the difference in h_{12} values for C23 and C24 on 20080607. These measurements were done on the same day, within 6 hours of each other and a distance of 15km apart on the European side of Istanbul (see Figure 6). A comparison of C23 and C24 illustrates the large effect of aerosol on the vertical profile of cloud microphysical properties. CDNC measured by the CDP for C23 were smaller than those measured for C24. CDNC in C23 reached 764 cm^{-3} at cloud base while those in C24 reached 1759 cm^{-3}. The corresponding CCN concentrations at a supersaturation of 0.3% were 583 and 631 cm^{-3} respectively. This is shown in Figure 37. In addition, CIP data shows that very large cloud droplets and raindrops were measured in C23 (see Figure 38) while in C24 large cloud droplets and raindrops were absent (see Figure 39). Instead ice hydrometeors and snow particles were measured and melted into rain drops. Although clouds C23 and C24 both precipitated, it is postulated that the predominant mechanisms involved in the formation of precipitation were altered and modified by the aerosol properties. This suggestion is supported by the proximity of the measurements in time and space, the similar airmass backtrajectories, the increased aerosol concentrations, increased CCN concentrations, modification of the r_e profile and modification of hydrometeors types. In addition, the decrease in r_e in C24 is consistent with the entrainment mixing as a significant thermodynamic process that modifies the r_e profile which in turn affects the coalescence efficiency and growth of precipitation sized particles. For example, the points identified as "activation of entrained air" in C23 were characterized by high droplet concentrations (CDNC > 20 cm^{-3}), small r_e that compare in size to those measured at cloud base were found within a strong updraft of 4.6 ms^{-1} 1390 m above cloud base. The cloud microphysical properties are similar to those of recently activated

particles found near cloud base. This suggests that aerosols entrained in the updraft are activated at a higher supersaturation than that present at cloud base and could have an effect on the linearity of the effective radius profile in convective clouds. This phenomenon was also observed in some other cases such as C6 and C12. Conant et al. (2004) have also made similar observations in Florida cumulus clouds.

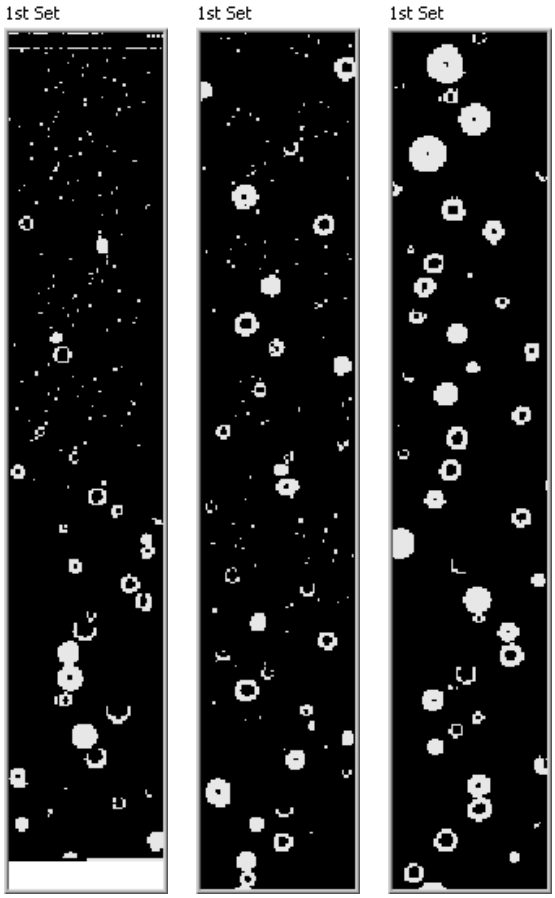

Figure 38. CIP images of cloud particles sampled during cloud penetrations in C23. Time is given in HH:MM:SS format. From left to right: 06:38:19, 4.6 °C, cloud depth 1021 m; 06:38:26, as before; 06:40:16, 6.8 °C, cloud depth 770 m. The width of each image strip is 1550 μm.

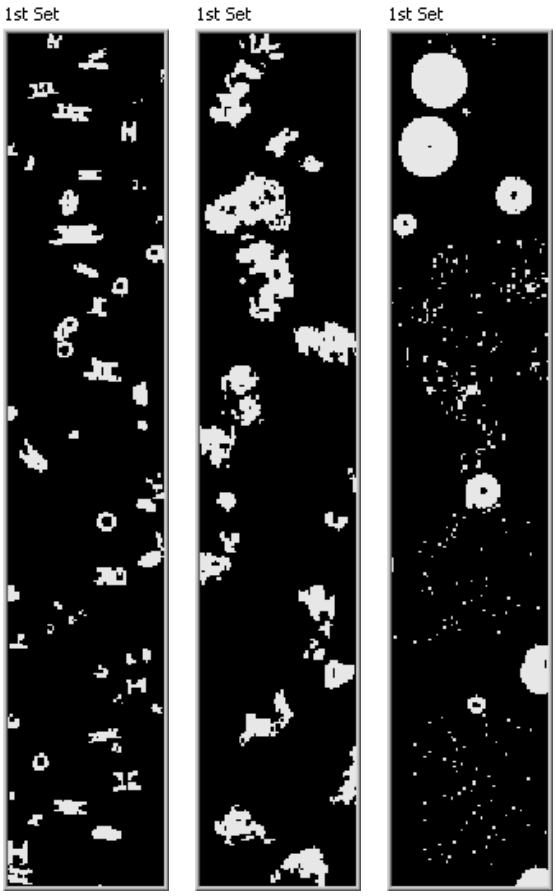

Figure 39. CIP images of cloud particles sampled during cloud penetrations in C24. Time is given in HH:MM:SS format. From left to right: 13:19:36, -0.6 °C, cloud depth 2572 m; 13:25:13, 0.5 °C, cloud depth 2247 m; 13:35:20, 6.7 °C, cloud depth 1101 m. The width of each image strip is 1550 μm.

7. CONCLUSION

Cloud physics aircraft have been employed to obtain detailed in situ measurements inside convective clouds in Texas, Saudi Arabia and Istanbul Turkey. The common goals of the field efforts were (1) to retrieve the aerosol size distribution below the bases of convective clouds to study the CCN activation properties and (2) to describe the physical chain of events and the microphysical properties of cloud processes that lead to precipitation formation within convective clouds. In this study 24 pairs of sub-cloud aerosol and cloud penetration data are studied. A total of 260 penetrations have been analyzed to provide information on the vertical distribution of cloud droplet effective radius and to provide insight on how aerosol particles are affecting cloud properties. The objectives of the study were (1) to identify typical aerosol size distributions at cloud base and to characterize the variability of the size distribution, (2) to examine the CCN activation of aerosols as a function of the aerosol size distribution, and (3) to provide information about the relationship between the droplet effective radius and the height above cloud base in different aerosol regimes.

Measurements of fine and coarse mode aerosol concentrations from the DMA, PCASP, CDP and FSSP instruments were combined and fitted with lognormal distributions. The fit parameters of the lognormal distributions are compared with cloud droplet effective radii. The modal analysis is a powerful tool in describing the structure of the ASD; however an attempt to relate the mode parameters to effective radius was unsuccessful. In general the relationships were observed to be weak and simplification

of the data set was needed. Cumulative concentrations were calculated integrating from the largest size in the ASDs to cutoff dry diameters of 1.1, 0.1 and 0.06 μm. The cumulative aerosol concentrations were found to be related with cloud condensation nuclei concentrations but not with maximum cloud base droplet concentrations.

Köhler Theory was used to predict CCN concentration. Ammonium sulfate was assumed to represent the soluble component of aerosol with dry sizes smaller than 0.5 μm and sodium chloride for aerosol larger than 0.5 μm. The measured CCN spectrum was used to estimate the soluble fraction. The correlations of the measured CCN concentration with the predicted CCN concentration were strong ($R^2 > 0.89$) for supersaturations of 0.2, 0.3 and 0.6%. The data points were below the 1:1 line indicating that the predicted CCN concentrations are lower than the measured CCN concentrations. The measured concentrations were typically consistent with an aerosol having a soluble fraction between roughly 0.5 and 1.0, suggesting a contribution of sulfate or some other similarly soluble inorganic compound. The predicted CCN were found to vary by ±3.7% when the soluble fraction was varied by 0.1. This is insignificant as it is much below the measurement uncertainty. In this analysis, the entire aerosol population was assumed to have a soluble component of either ammonium sulfate or sodium chloride. This is clearly a simplification, but it is a viable procedure despite the lack of information on chemical composition. The expected errors in this analysis are primarily associated with the instruments themselves and not the precise definition of the soluble species used to define the size resolved aerosol composition. The DMA's long sampling time relative to the wing mounted aerosol and cloud spectrometers introduces errors due

to the spatial resolution. Another concern is the performance of the PCASP and the method used to combine the DMA and PCASP aerosol size distributions. As Dusek et al. (2006) conclude, the critical supersaturation depends to first approximation on the soluble mass but to the third power on electrical mobility diameter. Therefore size distribution is by far the dominant factor in determining CCN.

This study has demonstrated that CCN-forced variations in cloud droplet number concentration can change the effective radius profile and the type of precipitation hydrometeors for two cases on 7 June 2008 in the vicinity of Istanbul. Though it is difficult to fully understand the mechanism by which aerosols effect precipitation, observed changes in convective cloud properties are due to a series of feedbacks that begin with changes in the size distribution of droplets that form on preexisting aerosol particles that act as CCN. Changes in the initial droplet size and vertical evolution of cloud droplets may induce changes at larger scales. The effects may propagate to cloud dynamics and to the overall size of clouds. These differences may have a major impact on the global hydrological cycle and energy budget.

REFERENCES

Ackerman, A. S., O. B. Toon, D. E. Stevens, A. J. Heymsfield, V. Ramanathan, E. J. Welton, 2000: Reduction of tropical cloudiness. *Science*, **288**, 1042-1047.

Albrecht, B.A., 1989: Aerosols, cloud microphysics and fractional cloudiness. *Science* **245**, 1227–1230.

Alpert, P., N. Halfon and Z. Levin, 2008: Does air pollution really suppress precipitation in Israel? *J. Appl. Meteorol. Climat.*, **47**, 933– 943.

Andreae, M. O., D. Rosenfeld, P. Artaxo, A. A. Costa, G. P. Frank, K. M. Longo, and M. A. F. Silva-Dias, 2004: Smoking rain clouds over the Amazon. *Science*, **303**, 1337–1342.

Birmili, W., A. Wiedensohler, J. Heintzenberg, and K. Lehmann, 2001: Atmospheric particle number size distribution in central Europe: Statistical relations to air masses and meteorology. *J. Geophys. Res.*, **106**(D23), 32,005–32,018.

Clarke, A. D., T. Uehara, and J. N. Porter, 1997: Lagrangian evolution of an aerosol column during the Atlantic Stratocumulus Transition Experiment. *J. Geophys. Res.*, **101**(D2), 4351–4362.

Conant, W. C., T. M. VanReken, T. A. Rissman, V. Varutbangkul, H. H. Jonsson, et al., 2004: Aerosol–cloud drop concentration closure in warm cumulus. *J. Geophys. Res.*, **109**, D13204, doi:10.1029/2003JD004324.

Cooper, W.A., 1988: Effects of coincidence on measurements with a Forward Scattering Spectrometer Probe. *J. Atmos. Ocean. Tech.*, **5**, 823-832.

Dusek, U., G. P. Frank, L. Hildebrandt, J. Curtius, J. Schneider, S. Walter, D. Chand, F. Drewnick, S. Hings, D. Jung, S. Borrmann, and M.O. Andreae, 2006: Size matters more than chemistry for cloud nucleating ability of aerosol particles. *Science*, **312**, 1375-1378.

Dye, J. E., and D. Baumgardner, 1984: Evaluation of the forward scattering spectrometer probe. Part I: Electronic and optical studies. *J. Atmos. Oceanic Technol.*, **1**, 329-344.

Freud, E., D. Rosenfeld, M. O. Andreae, A. A. Costa, and P. Artaxo, 2008: Robust relations between CCN and the vertical evolution of cloud drop size distribution in deep convective clouds. *Atmos. Chem. Phys. Discuss.* **5**, 10155–10195.

Hansen, J. E., M. Sato, and R. Ruedy, 1997: Radiative forcing and climate response. *J. Geophys. Res.*, **102**, 6831-6864.

Heintzenberg, J., 1978: Particle size distributions from scattering measurements of nonspherical particles via Mie-theory. *Contrib. Atmos. Phys.*, **51**, 91–99.

Heymsfield, A. J., and G. M. McFarquhar, 2001: Microphysics of INDOEX clean and polluted trade cumulus clouds. *J. Geophys. Res.* **106**(D22), 28653–28673, doi:10.1029/2000JD900776.

Hudson, J. G., and S. S. Yum, 2001: Maritime-continental drizzle contrasts in small cumuli. *J. Atmos. Sci.* **58**, 915–926.

Hussein, T., M. Dal Maso, T. Petäjä, I. K. Koponen, P. Paatero, P. P. Aalto, K. Hämeri, and M. Kulmala, 2005: Evaluation of an automatic algorithm for fitting the particle number size distributions. *Boreal Env. Res.* **10**, 337–355.

Jirak, I. L., and W. R. Cotton, 2006: Effect of air pollution on precipitation along the Front Range of the Rocky Mountains. *J. Appl. Meteorol.*, **45**, 236– 245.

Karstens, U., C. Simmer, and E. Ruprecht, 1994: Remote sensing of cloud liquid water. *Meteorol. Atmos. Phys.*, **54**, 157-171.

Kaufman, Y. L., and R. S. Fraser, 1997: The effect of smoke particles on clouds and climate forcing. *Science*, **277**, 1636–1639, 1997.

Levin, Z., A. Teller, E. Ganor, and Y. Yin, 2005: On the interactions of mineral dust, sea salt particles and clouds—A measurement and modeling study from the MEIDEX campaign. *J. Geophys. Res.,* **110,** D20202, doi:10.1029/2005JD005810.

Liu, P. S. K., W. R. Leaitch, J. W. Strapp, and M. A. Wasey, 1992: Response of Particle Measuring Systems airborne ASASP and PCASP to NaCl and latex particles. *Aerosol Sci. Technol.,* **16**, 83–95.

Markowski, G., 1987: Improving Twomey's algorithm for inversion of aerosol measurement data. *Aerosol Sci. Technol*., **7**, 127-141.

Pruppacher, H. R., and J. D. Klett, 1997. *Microphysics of Clouds and Precipitation.* Kluwer.

Ramanathan, V., P. J. Crutzen, J. T. Kiehl and D. Rosenfeld, 2001: Aerosols, climate, and the hydrological cycle. *Science*, **294**, 2119-2124.

Reid, J. S., H. H. Jonsson, H. B. Maring, A. A. Smirnov, D. L. Savoie, S. S. Cliff, E. A. Reid, M. M. Meier, O. Dubovik, and S. C. Tsay, 2003: Comparison of size and morphological measurements of coarse mode dust particles from Africa, *J. Geophys. Res.,* **108**(D19), 8593, doi:10.1029/2002JD002485.

Reist, P.C., 1984. *Introduction to Aerosol Science*. Macmillan Publishing Company.

Reutter, P., J. Trentmann, H. Su, M. Simmel, D. Rose, H. Wernli, M.O. Andreae, and U. Pöschl, 2009: Aerosol- and updraft-limited regimes of cloud droplet formation: Influence of particle number, size and hygroscopicity on the activation of cloud condensation nuclei (CCN). *Atm. Chem. and Phys. Disc.*, **9**, 8635-8665.

Roberts, G.C., and A. Nenes, 2005: A continuous-flow streamwise thermal-gradient CCN chamber for atmospheric measurements. *Aerosol Sci. Technol*., **39**, 206-221.

Rosenfeld, D., 2000: Suppression of rain and snow by urban air pollution. *Science*, **287**, 1793-1796.

——, and A. Givati, 2006: Evidence of orographic precipitation suppression by air pollution induced aerosols in the western U. S. *J. Appl. Meteorol.*, **45**, 893– 911.

——, R. Lahav, A. Khain, and M. Pinsky, 2002: The role of sea spray in cleansing air pollution over ocean via cloud processes. *Science*, **297**, 1667–1670.

——, and I. M. Lensky, 1998: Satellite-based insights into precipitation formation processes in continental and maritime convective clouds. *Bull. Amer. Meteor. Soc.,* **79,** 2457–2476.

——, U. Lohmann, G. B. Raga, C. D. O'Dowd, M. Kulmala, S. Fuzzi, A. Reissell, M. O. Andreae, 2008a: Flood or drought: How do aerosols affect precipitation? *Science*, **321**, 1309-1313.

——, Y. Rudich and R. Lahav, 2001: Desert dust suppressing precipitation - A possible desertification feedback loop. *Proceedings of the National Academy of Sciences*, **98**, 5975-5980.

——, W. L. Woodley, D. Axisa, E. Freud, J. G. Hudson, and A. Givati, 2008b: Aircraft measurements of the impacts of pollution aerosols on clouds and precipitation over the Sierra Nevada. *J. Geophys. Res.*, **113**, D15203, doi:10.1029/2007JD009544.

Salma, I., R. Ocskay, N. Raes, and W. Maenhaut, 2005: Fine structure of mass size distributions in an urban environment. *Atmos. Environ*. **39**, 5363-5374.

Seinfeld, J. H., and S. N. Pandis,1998: *Atmospheric Chemistry and Physics: From Air Pollution to Climate Change.* John Wiley & Sons, Inc.

Squires P., and S. Twomey, 1960: The relation between cloud droplet spectra and the spectrum of cloud nuclei. *Physics of Precipitation,* Amer. Geophys. Union, Geophys.Monogr. No. 5, 211-219.

Stolzenburg, M., N. Kreisberg, and S. Hering, 1998: Atmospheric size distributions measured by differential mobility optical particle size spectrometry. *Aerosol Sci. Technol.*, **29**, 402-418.

Tampieri, F., and C. Tomasi, 1976: Size distribution models of fog and cloud droplets in terms of the modified gamma function. *Tellus*, **28**, 332–347.

Tao, W. K., X. Li, A. Khain, T. Matsui, S. Lang, and J. Simpson, 2007: Role of atmospheric aerosol concentration on deep convective precipitation: Cloud-resolving model simulations. *J. Geophys. Res.,* **112,** D24S18, doi:10.1029/2007JD008728.

Teller, A., and Z. Levin, 2006: The effects of aerosols on precipitation and dimensions of subtropical clouds; a sensitivity study using a numerical cloud model. *Atmos. Chem. Phys.,* **6,** 67–80.

Twomey, S., 1959: The nuclei of natural cloud formation. Part II: The supersaturation in natural clouds and the variation of cloud droplet concentration. *Geofis. Pura. Appl.*, 43, 243-249.

—, 1965: The application of numerical filtering to the solution of integral equations encountered in indirect sensing measurements. *J. Franklin Inst.*, **279**, 95-109.

—, 1975: Comparison of constrained linear inversion and an iterative nonlinear algorithm applied to indirect estimation of particle-size distributions. *J. Comput. Phys.*, **18**, 188-200.

—, 1977: The influence of pollution on the shortwave albedo of clouds. *J. Atmos. Sci.*, **34**, 1149-1152.

van den Heever, S. C., G. G. Carrio, W. R. Cotton, P. J. DeMott, and A. J. Prenni, 2006: Impacts of nucleating aerosol on Florida convection. Part I: Mesoscale simulations. *J. Atmos. Sci.*, **63**, 1752-1775.

—, and W. R. Cotton, 2007: Urban aerosol impacts on downwind convective storms. *J. Appl. Meteor. Climatol.,* **46,** 828–850.

Warner, J., 1968: A reduction in rainfall associated with smoke from sugar-cane fires – An inadvertent weather modification? *J. Appl. Meteor.*, **7**, 247–251.

——, and S. Twomey, 1967: The production of cloud nuclei by cane fires and the effect on cloud droplet concentration. *J. Atmos. Sci*., **24**, 704-706.

Willeke, K., and K. T. Whitby, 1975: Atmospheric aerosols: Size distribution interpretation. *J. Air Pollut. Control Assoc*., **25**, 529-534.

Yin, Y., Z. Levin, T. G. Reisin, and S. Tzivion, 2000: The effects of giant condensation nuclei on the development of precipitation in convective clouds - A numerical study. *Atmos. Res.,* **53,** 91–116.

Yum, S. S. and J. G. Hudson, 2002: Maritime/continental microphysical contrasts in stratus. *Tellus,* **54B**, 61–73.

VITA

Name:	Duncan Axisa
Address:	4796 6th Street, Boulder, Colorado 80304
Email Address:	duncan.axisa@gmail.com
Education:	B.Ed., Education, University of Malta, 2000 B.S., Meteorology, Texas A&M University, 2002